frontiers in Earth Science

ORIGINAL RESEARCH
published: 26 November 2021
doi: 10.3389/feart.2021.779991

Genetic Mechanism and Environment Implications of Siderites in the Lopingian Coal-Bearing Series, Western Guizhou of China: Constrained by Whole-Rock and *In Situ* Geochemistry

Tianyang Yang[1,2], *Yulin Shen*[1,2]*, *Yong Qin*[1,2], *Yijie Zhang*[3], *Lu Lu*[1,2], *Jun Jin*[1,2,4], *Yong Zhao*[5], *Yulin Zhu*[1,2] *and Yunfei Zhang*[1,2]

[1]Key Laboratory of Coalbed Methane Resources and Reservoir Formation Process, Ministry of Education, Xuzhou, China, [2]School of Resources and Geosciences, China University of Mining and Technology, Xuzhou, China, [3]Sinopec Shengli Oilfield Administration Bureau Co., Ltd., Dongying, China, [4]Guizhou Engineering Technology Research Center for Coalbed Methane and Shale Gas, Guiyang, China, [5]Sinopec Xinjiang Xinchun Petroleum Development Co., Ltd., Dongying, China

OPEN ACCESS

Edited by:
Qiangtai Huang,
Sun Yat-sen University, China

Reviewed by:
Xia Guoqing,
Chengdu University of Technology, China
Yong Fu,
Guizhou University, China

***Correspondence:**
Yulin Shen
yulinsh@163.com

Specialty section:
This article was submitted to Geochemistry, a section of the journal Frontiers in Earth Science

Received: 20 September 2021
Accepted: 29 October 2021
Published: 26 November 2021

Citation:
Yang T, Shen Y, Qin Y, Zhang Y, Lu L, Jin J, Zhao Y, Zhu Y and Zhang Y (2021) Genetic Mechanism and Environment Implications of Siderites in the Lopingian Coal-Bearing Series, Western Guizhou of China: Constrained by Whole-Rock and In Situ Geochemistry. Front. Earth Sci. 9:779991. doi: 10.3389/feart.2021.779991

A large number of siderites have been found in the Lopingian (Late Permian) coal-bearing series in western Guizhou, which occurs in various microscopic morphologies and has potential insights into the sedimentary and diagenetic environments. An integrated set of analyses, such as microscopic observation; X-ray diffraction; whole-rock major and trace element, carbon, and oxygen isotope; and *in situ* major and trace element, has been carried out to unravel the genetic mechanism of the siderites and their environmental implications. According to the microscopic morphology, the siderites can be generally divided into three types and six subtypes, including gelatinous siderites (I), microcrystal-silty siderite [II; microlite siderites (II_1), powder crystal siderites (II_2)], and spheroidal siderite [III, petal-like siderite (III_1), radiating fibrous siderite (III_2) and concentric siderite (III_3)]. Whole-rock geochemical results show that the iron source for the formation of the siderites was mainly from extensive weathering of the Emeishan high-titanium basalts in hot climate conditions. The carbon and oxygen isotopic results indicate that the origin of CO_2 in type I siderites is derived from the dehydroxylation of organic matter. The CO_2 in types II_1 and II_2 siderites is mainly derived from deposited organic matter and marine carbonate rocks, respectively. The CO_2 source of type III siderites is sedimentary organic matter and marine carbonate rocks and is affected by different fluids during diagenesis. The whole-rock and *in situ* geochemical characteristics further point to that type I siderites were formed in the synsedimentary period most strongly affected by seawater. Redox proxies, such as V/Sc, V/(V+Ni), and δ Ce, constrained their formation in a stable and weakly reduced condition. Type II siderites could have been developed in saltwater. Among them, type II_1 siderites were formed in the early diagenetic stage, whereas type II_2 siderites originated from recrystallization of type II_1 siderites and accompanied by metasomatism with calcites under diagenetic fluids of weak reduction to weak oxidation conditions. Type III siderites were formed under the influence of multistage diagenetic fluids. Among them, type III_1

siderites formed by the growth of powder crystal siderites (II_2) under diagenetic fluids with a weak reducing condition. Type III_2 siderites formed by growth around microlite siderites under weak reducing diagenetic fluids. Type III_3 siderites formed by concentric growth in diagenetic fluids with weak reduction to weak oxidation conditions and relatively active conditions.

Keywords: siderites, sedimentary environments, diagenetic environments, coal-bearing series, Lopingian, western Guizhou

1 INTRODUCTION

Siderite is a common carbonate mineral, and sedimentary siderite is formed by complex reactions of iron and organic matter precipitated during quasi-syngenesis (Sánchez-Román et al., 2014; Wittkop et al., 2014; Weibel et al., 2016). Siderite mostly forms in sediments with organic-rich, low Eh (oxidation–reduction potential), weak oxidation to weak reduction conditions, high alkalinity, and low sulfur concentrations (Berner, 1981; Mozley, 1989; Haese et al., 1997; Uysal et al., 2000; Passey, 2014; Phillips et al., 2018; Hiatt et al., 2020). The geochemical characteristics of siderite have been used to characterize the porewater during diagenetic phases (Curtis et al., 1986; Mozley, 1989; El Albani et al., 2001; Passey, 2014; Hiatt et al., 2020), and the combination with other minerals can be used to distinguish marine and freshwater environments (Mozley and Wersin, 1992; Ludvigson et al., 1998; Choi et al., 2003; Lim et al., 2004; Rodrigues et al., 2015). For example, siderites in marine mudstones usually point to a rapid transgression in early diagenetic phase (Laenen and Craen, 2004). Moreover, the siderite morphology has been widely studied, and it is generally believed that cryptocrystalline siderite is mostly occurring in the marine environment, and authigenic spheroidal siderite is common in freshwater and organic-rich environment (Mozley, 1989; Laenen and Craen, 2004; Passey and Jolley, 2009; Passey, 2014; Weibel et al., 2016).

The siderite-bearing strata are widely developed in coal measures in western Guizhou, and some studies have been conducted to determine its characteristics, as well as the genesis (Shen et al., 2017; Shen et al., 2019; Zhang et al., 2018; Zhang et al., 2020). For example, various forms of siderite have been recently identified by Zhang et al. (2020), and the suggested morphology of siderites is controlled by sedimentary sequence. However, how the sedimentary and diagenetic environments control the formation of siderites has always been an extensively debated topic. In this article, we identified multiple siderite-bearing strata with variable micromorphological types of siderite at Lopingian coal-bearing series in Panxian, western Guizhou, China, and performed an integrated analysis on the samples and obtained a set of new petrological, mineralogical, and geochemical data. Based on these data, we analyzed the formation model of siderite and their implications for the depositional and diagenetic environment.

2 GEOLOGICAL BACKGROUND

The study area is located in Panxian, western Guizhou, at the junction of Yunnan and Guizhou, on the margin of an epicontinental basin covering South China (**Figure 1A**). During the late Permian, this area was in the Liupanshui fault depression (Xu and He, 2003). The Lopingian is a representative Upper Permian coal-bearing sequence in the region, and there are various sedimentary environments including continental, delta, and marine facies from west to east (Wang et al., 2011; Shen et al., 2016; Shen et al., 2019; Qin et al., 2018). Lopingian can be divided into Wuchiapingian and Changhsingian from bottom to top. The Wuchiapingian is mainly composed of gray, dark gray, and gray–yellow mudstones, silty mudstones, siltstones, fine sandstones, carbonate rocks, and coal seams. Multiple layers of marine key beds and regionally stable coal seams as products of pulsating transgression events can be used as good correlation marker beds (Wang et al., 2011; Shen et al., 2016). Meanwhile, the Changhsingian is mainly composed of gray and dark gray argillaceous siltstone, mudstone, limestone, and fine sandstone, with 6 to 20 coal seams (Shen et al., 2016). According to the sequence stratigraphic framework established by previous studies (Shao et al., 2011; Shen et al., 2016; Shen et al., 2019), the study strata can be divided into four third-order sequences.

The Y2 and Y3 drillings are located between Tucheng and Panzhou; Y3 drilling is located west of Panzhou (**Figure 1A**). The study strata are interpreted as delta, lagoonal tidal flat facies (Xu and He, 2003). Note that the siderite-bearing strata are usually grayish black to grayish yellow, which is different from the surrounding rock (**Figures 2A–C**). The main lithologies are mainly mudstone, silty mudstone, and few siltstones.

3 SAMPLES AND ANALYTICAL METHODS

A total of 25 siderite samples were taken from three drilling wells in the study area, among which J3 well samples were evenly distributed in the Late Permian coal-bearing series. To investigate the formation model of siderite and their implications for the sedimentary and diagenetic environments the following analytical methods were performed (**Figure 1B**).

The petrographical and mineralogical characteristics of the samples were detected by an Olympus BX53M microscope in the School of Resources and Geosciences, China University of Mining and Technology.

The whole-rock X-ray diffraction (XRD) analysis by X′ Pert Pro X-ray powder diffractometer was conducted in Regional Geology and Mineral Resources Institute of Hebei. The test conditions were as follows: (1) working voltage 40 kV; (2) working current 40 mA; (3) Cu-Kα ray, wavelength 0.15416 nm, Ni filter; and (4) continuous step scanning with a

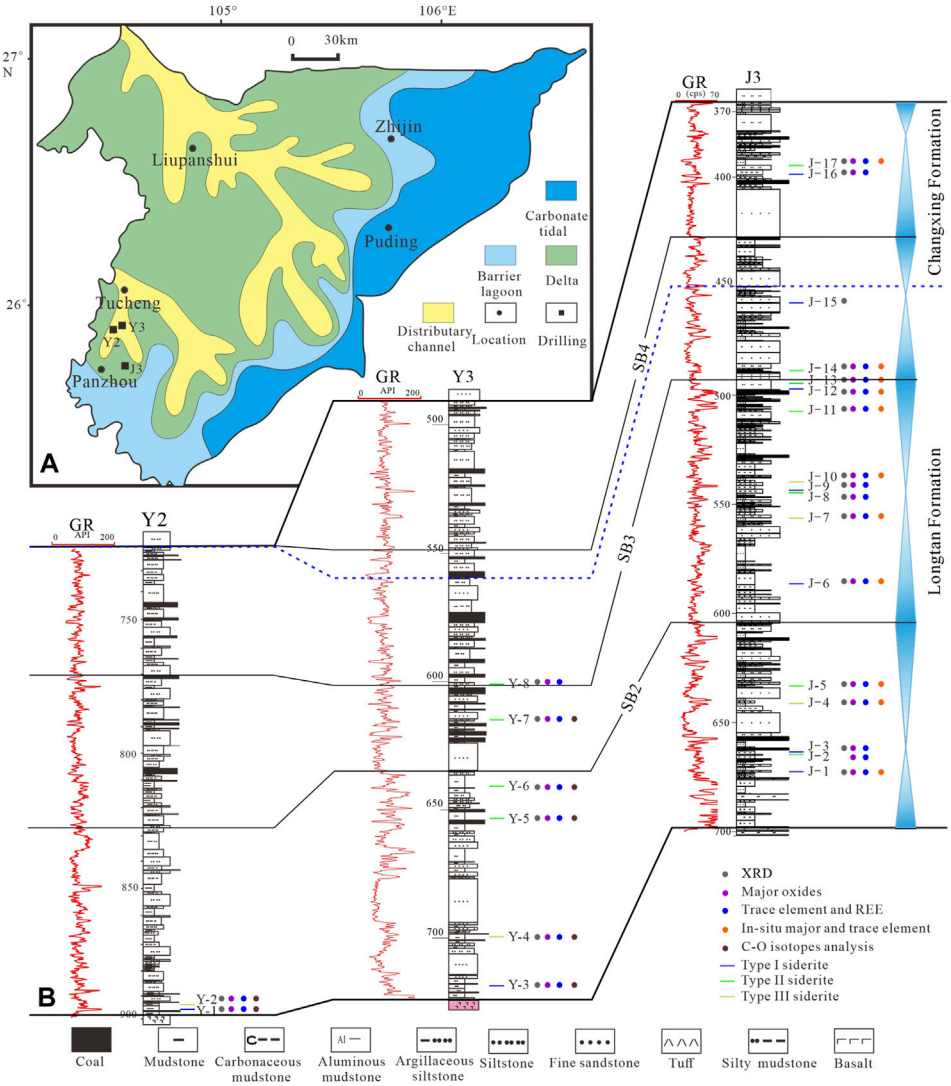

FIGURE 1 | (A): Lopingian sedimentary system and drillings location in western Guizhou (modified after Shen et al., 2016). **(B)**: Strata column, sampling positions, and analytical methods of J3, Y2, and Y3 wells.

step size of 0.017, the scanning speed is of 0.417782/s and the preset time is of 2′ 36″.

Whole-rock major element analyses were conducted on XRF (Primus II, Rigaku, Japan) at the Wuhan Sample solution Analytical Technology Co., Ltd., Wuhan, China. Detailed analysis procedure referred to "Methods for chemical analysis of silicate rocks-Part 28: Determination of 16 major and minor components" in the standard GB/T14506.28-2010.

Whole-rock trace element analyses were conducted on Agilent 7700e ICP-MS at the Wuhan Sample Solution Analytical Technology Co., Ltd., Wuhan, China. Detailed analysis procedure referred to "Methods for chemical analysis of silicate rocks-Part 30: Determination of 44 elements" in the standard GB/T14506.30-2010.

The samples for carbon and oxygen isotopic analysis were collected from Y2 and Y3 wells, and the analysis was conducted in the Geological and Environmental Institute of CUG (Wuhan). The siderite samples were first ground to less than 200-mesh and then reacted with phosphoric acid in a constant temperature tank at 72°C for 1 h. The collected CO_2 was transferred to the MAT-253 for the C-O isotopes analysis. The analysis precision better is than ±0.2‰.

In situ major and trace element analysis of siderite by LA-ICP-MS was conducted at the Wuhan Sample Solution Analytical Technology Co., Ltd., Wuhan, China. Laser sampling was performed using a GeolasPro laser ablation system that consists of a COMPexPro 102 ArF excimer laser (wavelength of 193 nm and maximum energy of 200 mJ) and a MicroLas optical system. Beam size of 32 μm and laser frequencies of 5 Hz were used during the analyses. An Agilent 7700e ICP-MS instrument was used to acquire ion-signal intensities. Each analysis incorporated a background acquisition of

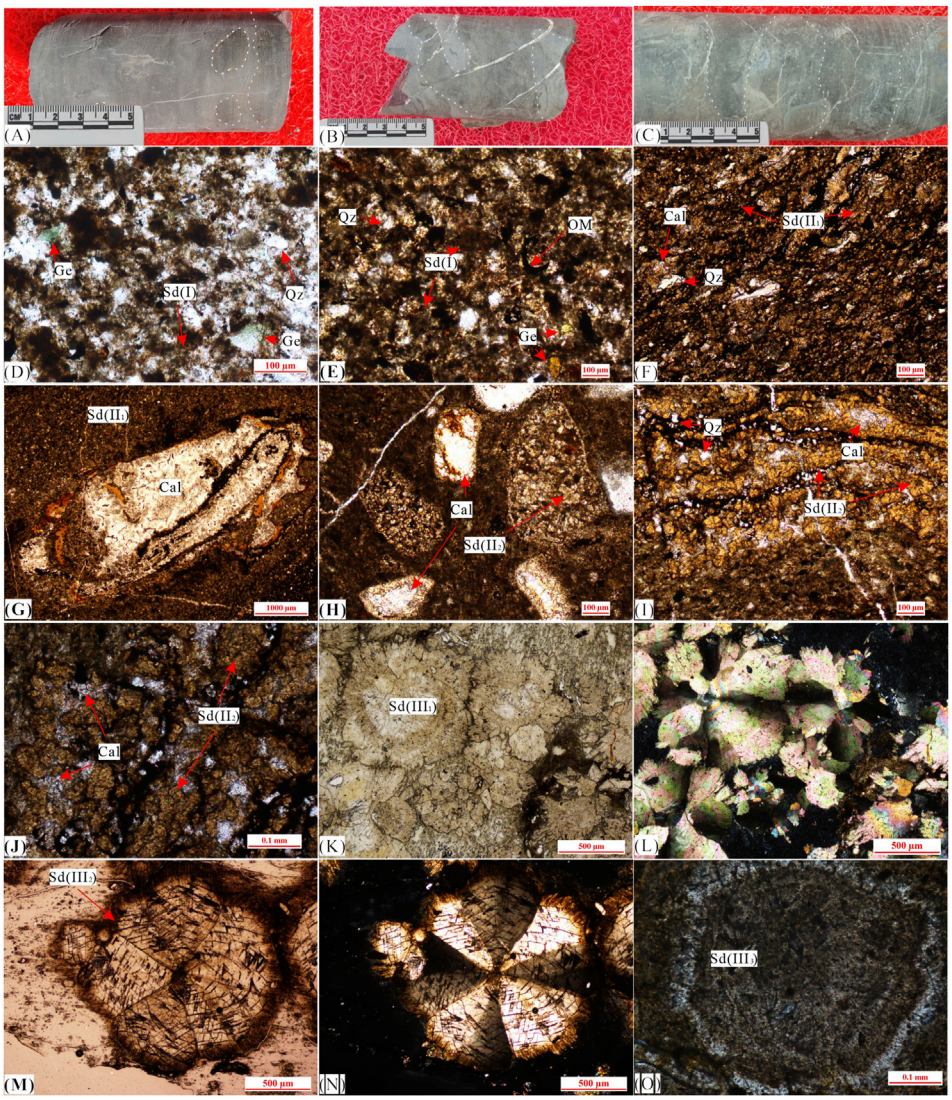

FIGURE 2 | Observation of drilling core and characteristics of siderites. **(A)** Siderite nodules and banded are discovered in the gray–black mudstone, J-3. **(B)** Siderite is lenticular and irregular agglomerated in the silty mudstone, J-7. **(C)** Irregular and banded siderite, J-11. **(D)** Gelatinous siderite mixed with clay minerals, showing angular glauconite, Y-3. **(E)** Gelatinous siderite is aggregated, and pyrite is locally developed, J-1. **(F)** Microlite siderite aggregate, evenly distributed, J-5. **(G)** Microlite siderite and powder crystal siderite are recrystallized around the shell of paleontology, J-13. **(H)** The paleontological shell is recrystallized into powder crystal siderite, J-14. **(I)** Powder crystal siderite, with large grains and developed to petal-like siderite, J-17. **(J)** Powder crystal siderite is recrystallized around calcite, and some are developed to petal-like siderite, Y-8. **(K)** Petal-like siderite, lane-polarized light, Y-2. **(L)** Cross-polarized light of "K." **(M)** Radiating fibrous siderite, lane-polarized light, Y-4. **(N)** Cross-polarized light of "M." **(O)** Concentric siderite, lane-polarized light, J-4. Sd, siderite; Qz, quartz; Ge, glauconite; OM, organic matter; Cal, calcite.

approximately 20 s followed by 50-s data acquisition from the sample.

4 RESULTS

4.1 Petrographic Characteristics

There are many siderite-bearing strata in western Guizhou, and the occurrence forms are diverse (**Figure 2**), mainly including nodular (**Figure 2A**), lenticular (**Figure 2B**), irregular (**Figures 2B,C**), and banded (**Figure 2C**). The banded siderite is usually surrounded by horizontal bedding and does not cut across the bedding (**Figure 2C**).

According to the microscopic morphology, the siderites can be generally divided into three types and six subtypes (**Figure 2**): gelatinous siderites (I), microlite siderites (II_1), powder crystal siderites (II_2), petal-like siderites (III_1), radiating fibrous siderites (III_2), and concentric siderites (III_3).

4.1.1 Gelatinous Siderite (I)

The gelatinous siderite is yellowish-brown under the polarizing microscope, and it is difficult to observe the grain boundary

TABLE 1 | Mineral compositions of the studied samples determined by XRD analysis (wt%).

Sample	Clays	Quartz	Siderite	Plagioclase	Calcite	Ankerite	Anatase	Pyrite	Hematite	Thenardite
J-1	17.0	20.6	49.4	—	5.3	—	5.2	—	—	2.4
J-3	9.0	38.6	37.4		6.3	—	8.7	—	—	—
J-4	77.6	13.0	3.06	3.4	—	—	2.9	—	—	—
J-5	16.6	18.0	62.8	—	—	—	2.6	—	—	—
J-6	13.5	37.4	28.2	—	1.9	16.8		—	2.3	—
J-7	19.4	11.2	66.7	1.7	1.0	—		—	—	—
J-8	11.0	52.0	23.6	1.3	5.1	—	6.8	—	—	—
J-9	21.0	39.1	31.1	1.4	—	—	7.4	—	—	—
J-10	20.0	23.6	48.2	2.8	—	—	5.4	—	—	—
J-11	16.4	39.6	23.9	3.0	1.3	—	6.0	—	—	9.7
J-12	42.8	26.3	21.7	4.7	—	4.5	—	—	—	—
J-13	14.9	8.2	72.3	—	1.6	—	—	3	—	—
J-14	23.4	13.3	50.8	—	—	—	—	2.4	—	—
J-15	19.4	23.2	12.0	—	—	42.8	—	—	2.6	—
J-16	9.0	39.1	10.9	4.5	11.2	11.5	12.0	1.8	—	—
J-17	16.5	26.1	42.6	1.7	12.1	1.0	—	—	—	—
Y-3	24.9	32.4	19.5	—	16.6	—	6.6	—	—	—
Y-4	3.6	4.4	90.7	—	1.4	—	—	—	—	—
Y-5	24.4	43.4	18.6	—	13.6	—	—	—	—	—
Y-6	16.3	12.4	57.9	—	13.4	—	—	—	—	—
Y-7	15.0	7.0	57.0	1.7	5.7	13.6	—	—	—	—
Y-8	3.0	9.4	77.7	—	9.9	—	—	—	—	—

(**Figures 2D,E**). Note that they were divided into two forms. One of which is evenly distributed in the pores between clastic particles, and the other is aggregated into blocks. Among them, uniform gelatinous siderite distributed in rocks is often filled in the pores between clastic particles in the form of cement and mixed with clay minerals (**Figure 2D**). The block-like gelatinous siderite is often surrounded by clastic particles, clay minerals, and organic matter (**Figure 2E**).

4.1.2 Microcrystal-Silty Siderite (II)

Crystal boundaries can be observed in microlite and powder crystal siderites under the microscope, which appear as hypidiomorphic or automorphic granular single crystal or aggregates with various shapes and sizes (**Figures 2F–J**). Among them, the microlite siderite often has color of light brown–yellow to light yellow, grain size between 0.004 and 0.03 mm, and mainly hypidiomorphic shapes. This kind of siderite is evenly distributed and mixed with clay minerals and organic matter or appears surrounding clastic particles (**Figure 2F**). The powder crystal siderite (II_2) is light yellow, and the grain size is between 0.015 and 0.09 mm with a good degree of crystallization. Siderite crystals are mainly automorphic and often develop at the edge of the cavity filled with calcite (**Figures 2G,H**) or in the area with high calcite content (**Figures 2I,J**).

4.1.3 Spheroidal Siderite (III)

This type of siderite has relatively large grain size, ranging from 0.1 to 1 mm, and appears light yellow to light yellowish brown under plane-polarized light (**Figure 2**). Although the petal-like siderite (III_1) has similar ring shapes, differences in morphology still exist. The fully developed siderite is spherical, and the incomplete siderite is bow-tie morphology (**Figure 2K**). Under cross-polarized light, the interference color is from pink to bright green (**Figure 2L**). Radiating fibrous siderite has a radiating texture, internal cleavage, and cross extinction under cross-polarized light (**Figures 2M,N**). Concentric siderite (III_3) has obvious concentric ring morphology (**Figure 2O**), and its distribution in the bedding is highly heterogeneous, usually concentrated in the form of aggregate.

XRD results show that the minerals in the samples include clay, quartz, siderite, plagioclase, calcite, ankerite, anatase, pyrite, hematite, and thenardite (**Table 1**). The siderite content ranges from 3.06 to 90.7 wt%. Other main components quartz, clay minerals, and calcite range from 4.4 to 52 wt%, 3 to 77.6 wt%, and 0 to 16.6 wt%, respectively. Other components are low, and some samples contain high ankerite. The content of type I siderite in rocks is relatively low. The XRD results show that the average content is only 26.3 wt%, with an exception of J-3 sample more than 40%. Type II siderite is common in rocks with high relative content (**Table 1**). The XRD analysis results showed that the average content in rocks reached up to 48.72% (**Table 1**). The distribution of spheroidal siderite in the rock is heterogeneous. The XRD analysis results show that the content varied largely among different samples (**Table 1**).

4.2 Whole Rock Geochemistry

4.2.1 Major Elements

The whole-rock major elements results are listed in **Table 2**. By normalizing the major elements results based on the upper crust (UC) (Taylor and McLennan, 1985), we find the concentration of main oxides in the studied samples is comparable to that in the UC, except the depletion of K_2O and the enrichment of TiO_2, *T*FeO (total iron), MnO, MgO, and CaO. The type I siderite-bearing samples have the highest content of SiO_2, and the samples containing the other two types of siderite are similar. All of

TABLE 2 | Statistics of major element oxide content (wt%), trace element, and rare earth element concentrations (μg/g) of the studied samples.

Sample	J-1	J-2	J-3	J-4	J-5	J-6	J-7	J-8	J-9	J-10	J-11	J-12	J-13	J-14	J-16	J-17	Y-1	Y-2	Y-3	Y-4	Y-5	Y-6	Y-7	Y-8
SiO_2	27.29	54.7	47.42	48.77	34.68	32.07	28.11	31.81	26.24	25.43	41.77	37.38	33.44	21.13	39.61	15.34	36.03	25.12	39.73	15.29	28.89	11.03	24.96	12
TiO_2	1.98	3.8	3.76	5.12	3.41	1.21	2.24	1.41	1.69	1.99	2.23	2.34	2.1	0.97	2.68	1.03	2.84	15.79	2.07	0.93	1.01	1.25	2.14	1.01
Al_2O_3	9.1	19	18.04	23.64	14.85	6.24	9.92	5.8	7.51	8.38	10.36	11.08	8.79	5.42	12.34	5.02	14.15	2.07	11.3	6.28	4.97	4.92	8.21	4.31
TFeO	33.74	9.46	14.36	7.98	22.6	26.91	34.42	34.27	35.43	35.4	23.87	25.71	27.72	35.15	21.18	43.57	26.77	32.19	17.25	47.13	27.68	38.72	25.05	39.17
MnO	0.72	0.03	0.18	0.03	0.26	0.66	0.86	0.69	0.65	0.6	0.4	0.27	0.38	0.5	0.36	1.21	0.27	0.17	0.56	0.3	1.24	1.04	0.42	0.59
MgO	1.51	1.09	1.18	1.5	1.56	3.88	2.16	3.68	3.76	3.91	3.32	4.3	4.42	5.64	3.96	3.2	1.05	0.52	0.9	1	1.81	3.16	3.54	2.96
CaO	4.04	0.96	1.74	0.39	1.06	6.06	1.81	2.46	3.16	2.39	2.23	3.02	3.38	5.23	4.94	3.24	5.93	0.72	9.18	1.48	7.04	5.93	7.05	5.54
Na_2O	0.34	0.6	0.58	1.04	0.67	0.49	0.63	0.14	0.32	0.47	0.74	0.81	0.74	0.26	0.68	0.29	0.08	0.17	0.22	0.09	0.15	0.23	0.47	0.16
K_2O	0.6	1.34	0.98	2.9	0.87	0.33	0.7	0.12	0.27	0.41	0.51	0.38	0.41	0.16	0.54	0.34	0.02	0.2	0.53	0.04	0.36	0.35	0.87	0.24
P_2O_5	0.36	0.43	0.42	0.11	0.28	0.64	0.3	0.35	0.38	0.42	0.21	0.48	0.53	0.64	0.91	0.38	0.35	0.3	0.28	0.22	0.77	0.97	0.42	0.5
LOI	20.05	8.3	11.02	7.46	19.75	20.88	19	19.7	20.66	20.97	14.3	14.29	17.49	24.05	12.39	26.63	11.73	22.21	17.49	26.52	25.77	31.67	26.59	31.16
SUM	99.73	99.69	99.69	98.96	99.98	99.37	100.14	100.42	100.06	100.36	99.93	100.06	99.41	99.15	99.58	100.24	99.22	99.44	99.5	99.29	99.68	99.27	99.71	97.64
CIA	83.69	84.77	85.84	81.68	82.49	76.07	77.72	90.79	84.7	80.69	77.61	78.2	75.28	84.18	81.33	79.11	97.92	95.38	89.68	94.95	84.92	81.16	76.82	84.38
Li	15.5	25.5	28	13.3	32	32.8	37	34.1	38.4	38.4	46.6	54.5	38.9	29.4	46.2	15	14.6	17	15.1	9.7	12.5	9.3	7.7	6.5
Be	2.6	3.4	3.4	5.5	3	1.9	2.7	2.2	2.5	3.3	2.5	1.9	2.3	2.1	2	2.8	1.4	3.8	2.9	2.9	2.8	2.9	2.4	3.4
Sc	16.2	27.8	24.8	32.3	22	11.9	18.6	15.9	20.5	20.4	17	21.6	14.6	10.8	19.1	13.2	23.5	14.3	15.4	11.2	9.4	13.3	14.7	17
V	169.4	325.1	297.8	357.1	260.6	109.6	206.1	151.2	199.5	220	194.5	213.2	166.3	153.4	221	126.1	391.1	147.8	153	93	137.9	86.9	158.8	118.9
Cr	72.5	105.3	123.2	227.3	72.7	62.3	73.8	37.9	55	75.9	105.1	157.2	108.1	79.2	89.5	38.6	63.9	41.7	62.5	17.1	33.5	60.1	143.7	37.2
Co.	49.2	30.4	36.9	22.2	39.5	15.4	57.7	22.2	26.5	28	33.2	21	26.4	20.1	31.6	67.3	84.5	45.2	38.7	51.6	11.2	31.6	22	76.1
Ni	53.3	71.9	81.2	67.7	53.1	31.5	81.6	61.9	67.8	65.8	97.2	89	71	46.8	118.3	47.7	44.1	42.1	49	47.4	11.3	30.8	33.6	57.1
Cu	92.3	193.5	187	212.6	146.9	35.6	99.3	63.9	71	83.1	85.5	79.7	85.3	30.9	113.3	51.1	105	60.5	101.5	38.1	40.1	51.5	70.7	45.7
Zn	81.5	133.4	168.2	158.9	130.8	61.3	150.3	71.7	76.6	88.3	96.8	120.4	89.9	54.3	111.9	115.2	197.8	130.5	173.8	302.1	49.6	81	105.6	221.1
Ga	18	35.3	34.2	41.8	27.1	11.3	20.6	13.4	15	16.7	19.6	21.6	16.3	11.1	23.6	9.9	31.7	32.4	21.2	19.6	9.3	9.4	15.6	6.4
Rb	22.7	46.7	36.2	88.5	28.2	11.4	22.7	4.6	9.5	13.7	17.5	14.3	14.4	5.5	20.1	12.2	1.8	9.6	25.3	3.7	14.6	13.7	33.3	8
Sr	180.2	276.8	248.8	441	229.5	224.2	243.3	102	241.5	150.9	198.2	195.9	155.8	159.5	365.1	138.5	190.9	199.1	140.1	64.2	148.8	145.1	234.2	181.3
Zr	250.7	574	492.3	592	361.8	159.7	238.2	157.3	185.7	222.6	271.9	251.6	235.7	130.7	358.8	137.5	196.1	463.2	359	124.9	147.1	163.8	193.9	194
Nb	41.3	87.5	77.6	75	51.1	22.4	32.8	18.9	24.3	29.5	41.6	38.7	36.9	18.7	39.3	17.7	25.5	48.7	46.2	15	17.5	21.4	28.5	14.3
Sn	2	4.1	3.8	4.5	3	1.2	2.2	1.3	1.5	1.8	2.3	2.2	1.8	1.2	2.7	1.1	1.7	4.9	2.7	1.1	1	0.9	1.5	
Cs	0.7	1.8	1.6	3.1	1.3	0.3	0.7	0.2	0.3	0.5	0.8	0.5	0.5	0.2	0.5	0.4	0	0.3	0.6	0.2	0.4	0.4	0.8	0.3
Ba	136.6	341	275.3	1,142.9	459.4	144.7	341	135.9	171.6	263.8	257.7	169.7	215.2	107.2	167.4	167.2	140.5	184.5	122.5	103	193.4	223.7	354.6	224.1
Hf	6.2	14	12.3	15.6	8.7	4	6	3.6	4.3	5.2	6.7	6.2	5.8	3.2	8.2	3.1	5.8	11.5	9	3.3	3.9	4.3	5.4	4.6
Ta	2.3	5.4	5	4.4	3.1	1.4	2	1.1	1.4	1.8	2.4	2.2	2.1	1.1	2.3	1.1	2.3	3.9	3.7	1.2	1.4	1.7	2.2	1
Tl	0.1	0.2	0.3	0.2	0.1	0	0	0	0	0	0.1	0	0.1	0	0.1	0	0	0	0	0	0	0	0.1	0
Pb	4.5	8.7	7.8	13.8	6.2	4.1	4.3	3.3	4.8	3.3	7.9	2.3	7.3	4.5	6.1	3.5	10.3	21	11.3	12.9	2.9	4.9	4.4	8.5
Th	6.2	16	13.6	16.7	8.4	3.9	5.7	3.3	4.2	5	7.1	6.1	6.1	3.6	8.5	3.2	5.3	13.7	10.1	3.3	4.6	4.6	5.2	3.8
U	1.4	3.7	3.2	3.7	1.9	1.8	1.2	0.8	1	1.1	1.4	1.4	1.4	1.5	1.6	0.8	1.5	2.5	2.3	1.1	1.9	1	1.2	0.8
La	44	93.4	82.5	118.3	50.9	39	43.5	25.1	30.9	37.7	43.6	38.6	40	32.2	61.7	21.6	35.8	54.3	68	18	38	40.8	32.9	31.4
Ce	86.5	201.1	176	228.9	110.8	79	89.7	52.4	63.4	74.8	87.8	83.7	84.4	69.2	139	47.1	102.4	125.6	144.9	39.8	78.4	90.5	68.5	66.3
Pr	10.6	24	21	26	14	9.4	10.9	6.4	7.8	9	10.2	10.4	10	8.4	17.4	5.6	13.5	15	15.3	5.5	11.5	12.3	9.1	8.5
Nd	42.3	91	82.9	95.1	55	39.6	45.1	27.9	33.6	38.8	39.5	44.2	42.1	36	76.8	24.3	57.9	59.9	68.5	23.9	53.1	54.4	38.4	35.5
Sm	8.9	15.8	15.5	13.8	11.3	8.4	8.2	6.9	7.9	9.2	7.6	10.7	9.6	8.5	18.6	6.1	15	14.6	12.6	6.3	16.1	12.4	8.6	7.9
Eu	3	3.7	4.2	2.9	3.2	2.7	2.3	2.4	2.6	2.9	2.4	3.7	3.2	3.5	6	1.7	4.9	3.7	3.3	2.1	5.7	4.2	2.8	2.4
Gd	7.9	12.4	14	9.4	10	7.2	7.4	7.9	8.5	8.7	7.5	10.8	9.2	8.9	16	6	15.5	15.2	12.8	7.1	17.6	11.3	8.7	6.9
Tb	1.1	2	2.1	1.7	1.6	1	1.2	1.1	1.2	1.2	1.2	1.3	1.3	1.2	1.9	0.9	2.6	2.6	1.8	1.2	2.3	1.4	1.3	1.1
Dy	6.6	11.2	11	10.8	8.8	5	7	5.8	5.9	6.6	6.5	6.7	6.2	6.4	9.4	5.1	13.6	15.5	9.4	7.3	10.8	6.3	6.6	6.2
Ho	1.1	2.2	2	2.2	1.7	0.8	1.4	1.1	1.1	1.1	1.2	1.1	1	1.1	1.5	0.9	2.3	2.9	1.6	1.4	1.8	1	1.2	1.2
Er	3.2	5.9	5.3	6.3	4.5	2.2	3.9	3	3	3.2	3.2	3	2.8	2.7	3.9	2.6	5.8	8.4	4.5	3.7	4.7	2.7	3.1	3.4
Tm	0.4	0.8	0.7	0.9	0.6	0.3	0.5	0.4	0.4	0.4	0.4	0.4	0.4	0.4	0.5	0.3	0.8	1.4	0.7	0.6	0.7	0.4	0.5	0.6
Yb	2.8	5.2	4.5	5.8	3.6	1.6	3.3	2.5	2.6	2.4	2.6	2.4	2.2	2.2	3.1	2.3	4.8	9	4.1	3.6	4.3	2.2	2.9	3.2
Lu	0.4	0.7	0.6	0.8	0.5	0.2	0.5	0.4	0.4	0.4	0.4	0.4	0.3	0.3	0.5	0.3	0.7	1.4	0.6	0.6	0.7	0.3	0.4	0.5
Sr/Ba	1.3	0.8	0.9	0.4	0.5	1.6	0.7	0.8	1.4	0.6	0.8	1.2	0.7	1.5	2.2	0.8	1.4	1.1	1.1	0.6	0.8	0.7	0.7	0.8
V/Cr	2.3	3.1	2.4	1.6	3.6	1.8	2.8	4	3.6	2.9	1.9	1.4	1.5	1.9	2.5	3.3	6.1	3.5	2.5	5.4	4.1	1.4	1.1	3.2
V/(V + Ni)	0.8	0.8	0.8	0.8	0.8	0.8	0.7	0.7	0.8	0.8	0.7	0.7	0.7	0.8	0.7	0.7	0.9	0.8	0.8	0.7	0.9	0.7	0.8	0.7
V/Sc	10.4	11.7	12	11.1	11.9	9.2	11.1	9.5	9.7	10.8	11.5	9.9	11.4	14.2	11.6	9.6	16.7	10.3	10	8.3	14.7	6.5	10.8	7
Sr/Cu	2	1.4	1.3	2.1	1.6	6.3	2.5	1.6	3.4	1.8	2.3	2.5	1.8	5.2	3.2	2.7	1.8	3.3	1.4	1.7	3.7	2.8	3.3	4
δ Ce	−0.05	−0.02	−0.03	−0.04	−0.03	−0.05	−0.04	−0.05	−0.05	−0.06	−0.04	−0.04	−0.04	−0.04	−0.03	−0.03	0.02	0	−0.03	−0.05	−0.09	−0.05	−0.06	−0.05
ΔEu	1.08	0.77	0.86	0.74	0.89	1.02	0.9	0.99	0.98	0.97	0.97	1.04	1.04	1.21	1.03	0.83	0.97	0.76	0.78	0.95	1.04	1.06	0.97	0.96

$\delta\ Ce = lg(3*Ce_N)/(2*La_N+Nd_N)$.

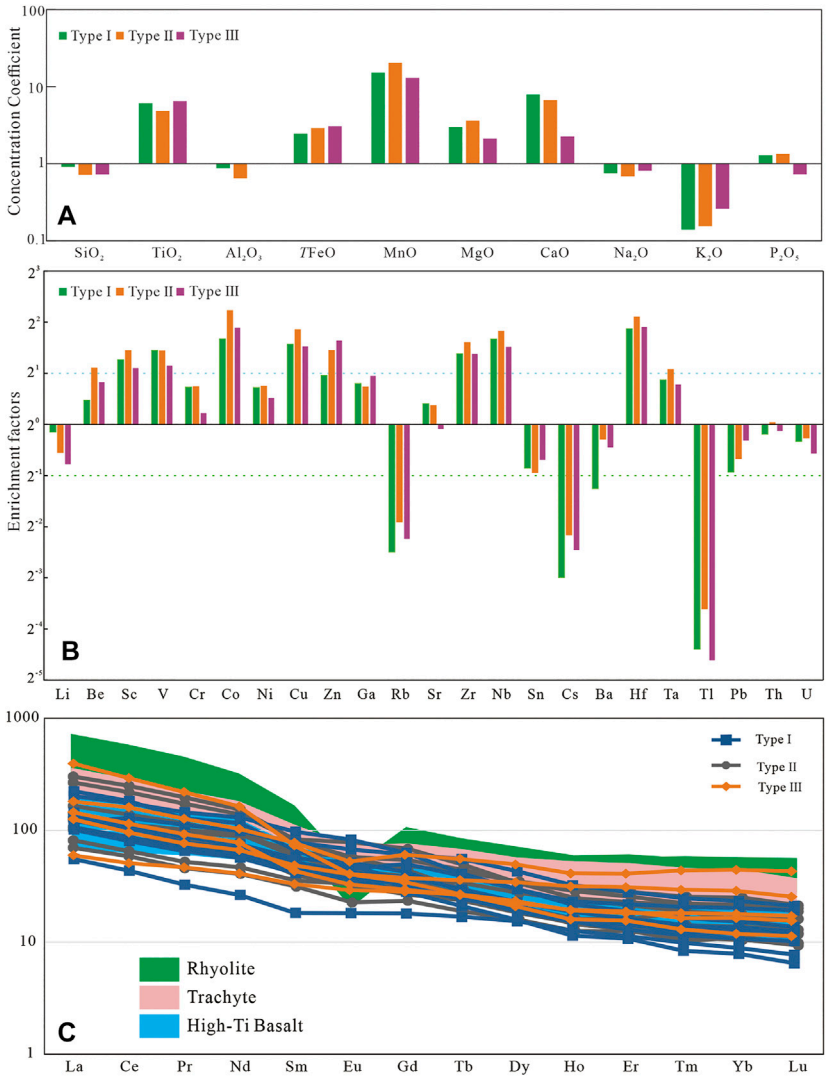

FIGURE 3 | (A) Major elements concentration coefficients (CC) of the studied samples, normalized by the UC. **(B)** Enrichment factors of trace elements of different types of siderite; **(C)** REE distribution pattern of different types of siderite. The pink and green areas are for trachyte and rhyolite (Xu et al., 2010), and the blue area is for high-Ti basalt (Xiao et al., 2004).

siderite-bearing samples have a high content of TiO_2, MgO, and MnO, which is likely related to the provenance. In addition, the *T*FeO content of samples containing type I siderite is the lowest, and the content of CaO gradually decreases from Samples containing type I to those containing type III.

4.2.2 Trace Elements

For most sedimentary deposits, some trace elements and aluminum can be well preserved and transported along with clastic materials and are usually immobile during diagenesis. These elements can be used for paleoenvironmental reconstruction only if their contents deviate greatly from average shale and have a good correlation with Al (Tribovillard et al., 2006). The enrichment factors of elements [$EF_{element\ X} = X/Al_{sample}/(X/Al_{average\ shale})$] are obtained by Al normalization, and the results are shown in **Figure 3B** (Tribovillard et al., 2006). Among them, the enrichment factors of Cr, Ni, Ga, Sr, Ba, Th, and U are between 0.5 and 2, close to the average shale. Th, Ga, and U have a good positive correlation with Al, whereas Sr, Ba, Ni, Cr, and Rb have a poor correlation (**Figure 4**).

4.2.3 Rare Earth Elements

The ΣREE values of the siderite-bearing samples are relatively high varying between 121 and 523 ppm. **Figure 3C** shows the distribution pattern of REE. The REE distribution pattern of all samples shows a significant enrichment of LREE. By comparing them with the values of the high-titanium basalts, trachytes, and rhyolites in the study area (Xiao et al., 2004; Xu et al., 2010) (**Figure 3C**), it was found that all samples are similar to the high-titanium basalts. The δ Ce values [$\delta\ Ce = lg\ (3 * Ce_N)/(2 * La_N + Nd_N)$] range from −0.09 to 0.02, whereas δ Eu

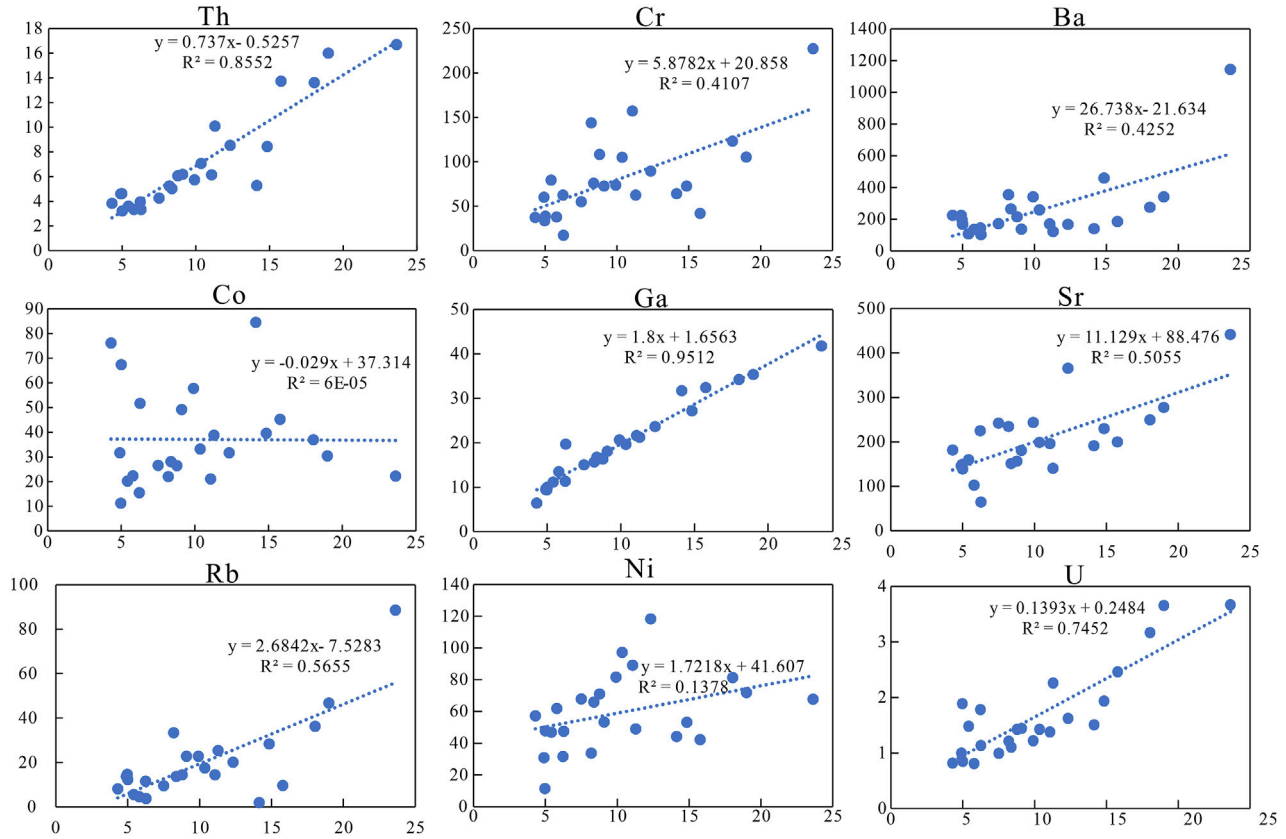

FIGURE 4 | Covariant relationship between Al and some trace elements, in which Th, Ga, and U are positively correlated with Al.

TABLE 3 | The results of carbon–oxygen isotope.

Sample	Siderite type	$\delta^{13}C‰$ (PDB)	$\delta^{18}O_{SMOW‰}$
Y-1	I	−10.06	17.34
Y-2	III	−6.33	28.38
Y-3	I	−9.20	20.65
Y-4	III	−11.94	25.78
Y-5	II	−10.58	23.23
Y-6	II	−2.80	24.64
Y-7	II	−4.01	23.31

values of samples with different types of siderite are different (**Table 2**). Most samples containing gelatinous siderite have δ Eu value larger than 1, whereas samples with type II siderite have δ Eu greatly variable from 0.77 to 1.04, (**Table 2**). The samples with type III siderite have δ Eu values ranging from 0.76 to 0.97, indicating slightly negative anomalies in element Eu.

4.3 Carbon–Oxygen Isotopic Compositions

The results of carbon–oxygen isotopes are shown in **Table 3**. The samples with type I siderite have uniform $\delta^{13}C_{PDB}$ and $\delta^{18}O_{SMOW}$ values of −9.20‰ to −10.06‰ and 17.34‰ to 20.65‰, respectively. The $\delta^{13}C_{PDB}$ values of samples with type II siderite range greatly from −2.80‰ to −10.58‰, which are dependent on the crystal types. The $\delta^{18}O_{SMOW}$ values are similar ranging from 23.23% to 24.64‰. The samples with type III siderite have $\delta^{13}C_{PDB}$ and $\delta^{18}O_{SMOW}$ of −6.33‰ to −11.94‰ and 25.78‰ to 28.38‰, respectively, with large fluctuation.

4.4 *In Situ* Geochemistry

The detailed results are shown in **Supplementary Appendix S1**, and the *in situ* spots are shown in **Figures 5**, **6**. Among them, the type I siderite has $FeCO_3$ (wt%) ranging from 26.62% to 51.64%, with an average of 36.63%, average $CaCO_3$ of 3.56%, and average $MgCO_3$ of 6.76%. For microlite siderite, the content of $FeCO_3$ (wt %) ranges from 47.34% to 86.8%, with an average of 72.67%. The contents of $CaCO_3$ and $MgCO_3$ vary greatly in different samples. The average content of $CaCO_3$ and $MgCO_3$ in J-5 is 4.43% and 2.79%, whereas that in J-11 is 7.64% and 7.99%, and that in J-13 is 8.58% and 10.27%, respectively. The environment formed by microlite siderite may be more extensive than that of gelatinous. The content of $FeCO_3$ (wt%) in powder crystal siderite ranges from 64.11% to 90.68%, with an average of 76.39%; the content of $CaCO_3$ ranges from 5.62% to 11.22%; and the content of $MgCO_3$ ranges from 2.76% to 16.76%, which are similar to the results of microcrystalline siderite samples. The content of $FeCO_3$ in type III siderite ranges from 71.26% to 91.87%, and the contents of $CaCO_3$ and $MgCO_3$ are lower than those in the other two types of siderite.

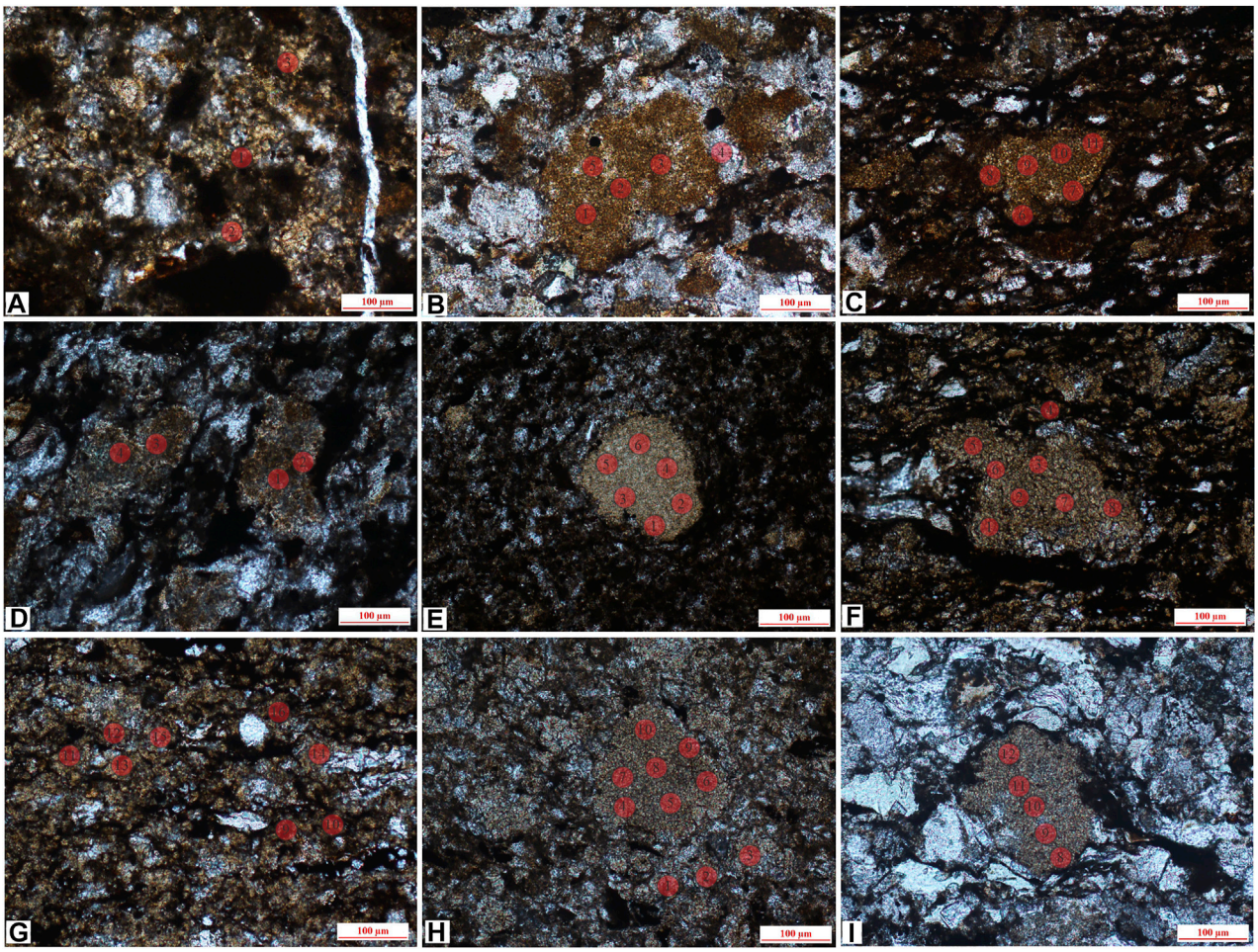

FIGURE 5 | *In situ* sites of gelatinous siderite and microlite siderite, **(A)** J-1, gelatinous siderite and partly recrystallized into powder crystal siderite (lane-polarized light); **(B,C)** J-6, mass aggregate, distributed among debris particles (lane-polarized light); **(D)** J-12, siderite is evenly distributed (lane-polarized light); **(E)** J-16, mass aggregate siderite and evenly distributed gelatinous siderite (lane-polarized light); **(F,G)** J-5, uniform distribution, microlite siderite (lane-polarized light); **(H)** J-11, microlite siderite is evenly distributed (lane-polarized light); **(I)** J-10 (1), mass microlite siderite is distributed between clastic particles (lane-polarized light).

The Sr/Ba value of type I siderite ranges from 0.79 to 3.75, with an average of 2.26, higher than that of the whole rock. δ Ce is between −0.08 and 0.06, with an average of 0.01; V/(V+Ni) is between 0.58 and 0.90, with an average of 0.73; and V/Cr is between 1.34 and 11.12, with an average of 2.36, which are also close to the whole rock. The V/Sc value is higher than the whole rock, with an average of 35.85. Different samples of type II_1 siderite are different in composition, although the *in situ* results are similar to that of the whole rock. The Sr/Ba value of type II_2 siderite ranges from 0.38 to 1.66, with an average of 0.58, which is quite different from the whole rock. There is little difference in Sr/Ba values of type III siderite, and the total average value is 0.50. The δ Ce value is between −0.19 and 0, and types III_1 and III_2 are different, reflecting the different diagenetic water where type III siderite formed. The V/(V+Ni), V/Cr, and V/Sc of III_1 and III_2 are also different.

5 DISCUSSION

5.1 Provenance Analysis of Siderite-Bearing Strata

The abundance of trace elements and the ratio of some immobile elements such as Al_2O_3/TiO_2, ΣREE, and La/Yb in mudstone can help to perform provenance analysis (Spears and Rice, 1973; McLennan et al., 1993; He et al., 2007; Dai et al., 2017; Xie et al., 2018; Liu et al., 2020). Rare earth elements are not easy to migrate during sedimentation and diagenesis, and the distribution pattern of REE can be used for provenance analysis (Boynton, 1984; Dai et al., 2017; Liu et al., 2019). **Figure 3C** shows that the REE distribution curves of all of siderite-bearing strata samples are relatively similar, which are characterized by enrichment in LREE and depletion in HREE. Eu has no obvious anomaly similar to Emeishan high-titanium basalt (Xiao et al., 2004). To study the provenance of the siderite-bearing strata, the discrimination

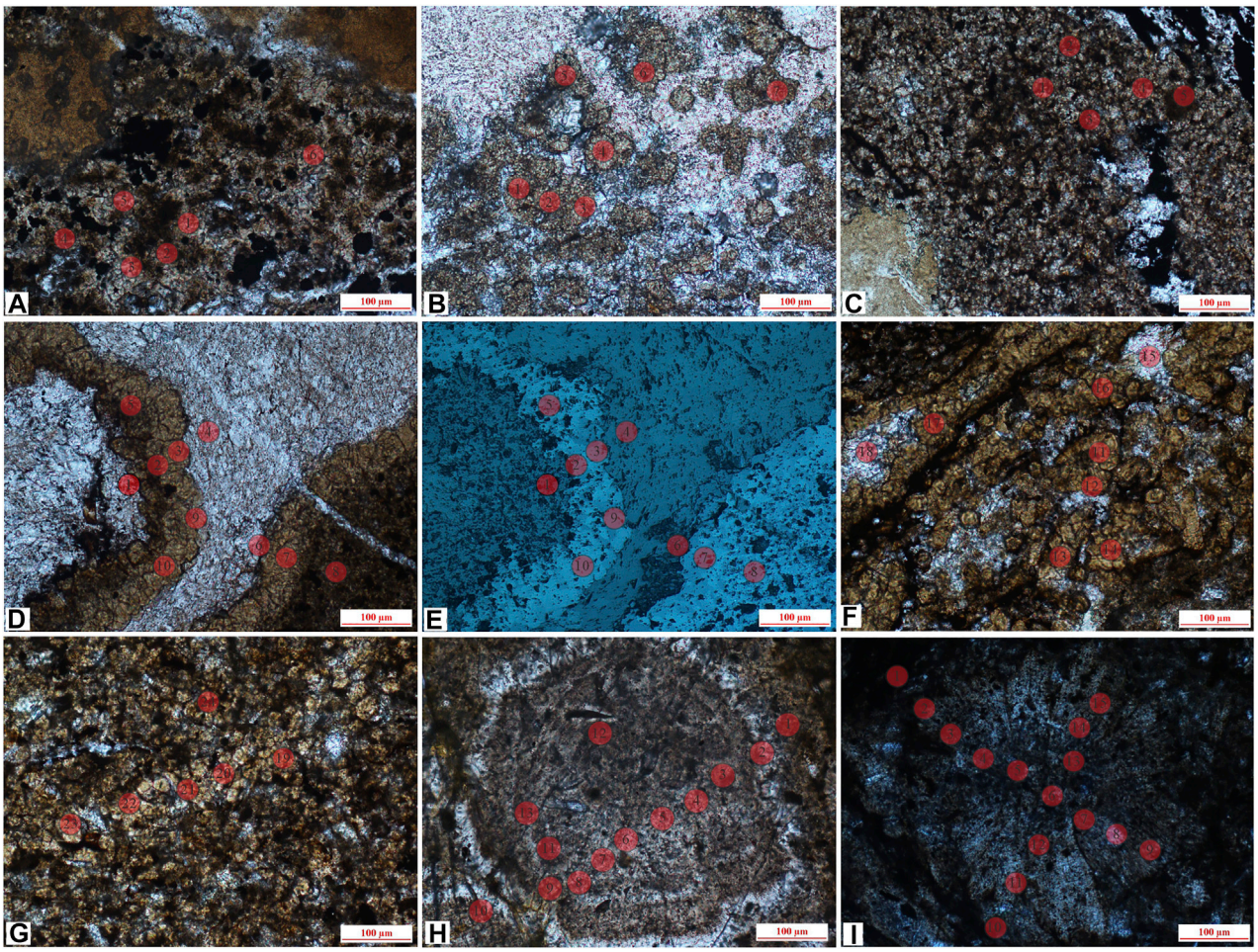

FIGURE 6 | *In situ* sites of microlite siderite, powder crystal siderite and sphaerosiderite, **(A)** J-13, microlite siderite, surrounded by clay minerals (lane-polarized light); **(B)** J-10 (2), powder crystal siderite, partially developed to petal-like siderite (lane-polarized light); **(C)** J-14, the powder crystal siderite is evenly distributed (lane-polarized light); **(D)** J-17 (1), powder crystal siderite and calcite (lane-polarized light); **(E)** reflecting light of **(D)**; **(F)** J-17 (2), powder crystal siderite, partially developed to petal-like siderite (lane-polarized light); **(G)** J-17 (3), powder crystal siderite (lane-polarized light); **(H)** J-4, concentric siderite (lane-polarized light); **(I)**. J-7, petal-like siderite (lane-polarized light).

diagram of ΣREE versus La/Yb was applied (Allègre and Michard, 1974; Xie et al., 2018) (**Figure 7A**). Apart from a small number of samples with gelatinous siderite that fall within the region of sedimentary rock, the others fall in the alkaline basalt (**Figure 7A**). Positive Eu anomalies indicate the existence of a large amount of mafic rock detritus, whereas strong negative Eu anomalies indicate the incorporation of felsic magmatic material (Dai et al., 2017; Liu et al., 2020). Al_2O_3/TiO_2 is also a reliable index used to discriminate the provenance of sedimentary rocks (Spears and Rice, 1973; He et al., 2003; He et al., 2007; Dai et al., 2017; Liu et al., 2020), and previous studies have suggested that Al_2O_3/TiO_2 <7 is characteristic of the Emeishan high-titanium basalt (He et al., 2007). **Figure 7B** shows that the δ Eu value of samples ranges from 0.74 to 1.21, and Al_2O_3/TiO_2 values are less than 7, falling in or similar to the field of Emeishan high-titanium basalt (Xiao et al., 2004; Dai et al., 2016; Liu et al., 2020). The high-titanium basalt in the east of Emeishan Large Igneous Province located in the Kangdian Upland is the most likely provenance area of the Late Permian coal-bearing strata in western Guizhou (Chung and Jahn, 1995; Xiao et al., 2004). During Late Permian, the South China was hot and humid (Bercovici et al., 2015; He et al., 2020; Zhang et al., 2020). In this case, the source rock suffered strong chemical weathering, and the iron was continuously leached under strong weathering and brought into the sedimentary basin after frequent regression and transgression, providing a sufficient iron source for the formation of siderite.

There are two major possible sources of carbon in sedimentary rocks: sedimentary organic matter and marine carbonate rocks (Ohmoto, 1972; Veizer et al., 1980; Liu et al., 2021). The CO_2 source was determined based on the discrimination diagram of $\delta^{13}C_{PDB}$ versus $\delta^{18}O_{SMOW}$ (**Figure 8**). The data of gelatinous siderite indicate that the source of CO_2 was derived from the dehydroxylation of organic matter, and its formation was affected by seawater and organic matter. The data distribution of microcrystal-silty siderite (II) is scattered, and its CO_2 source

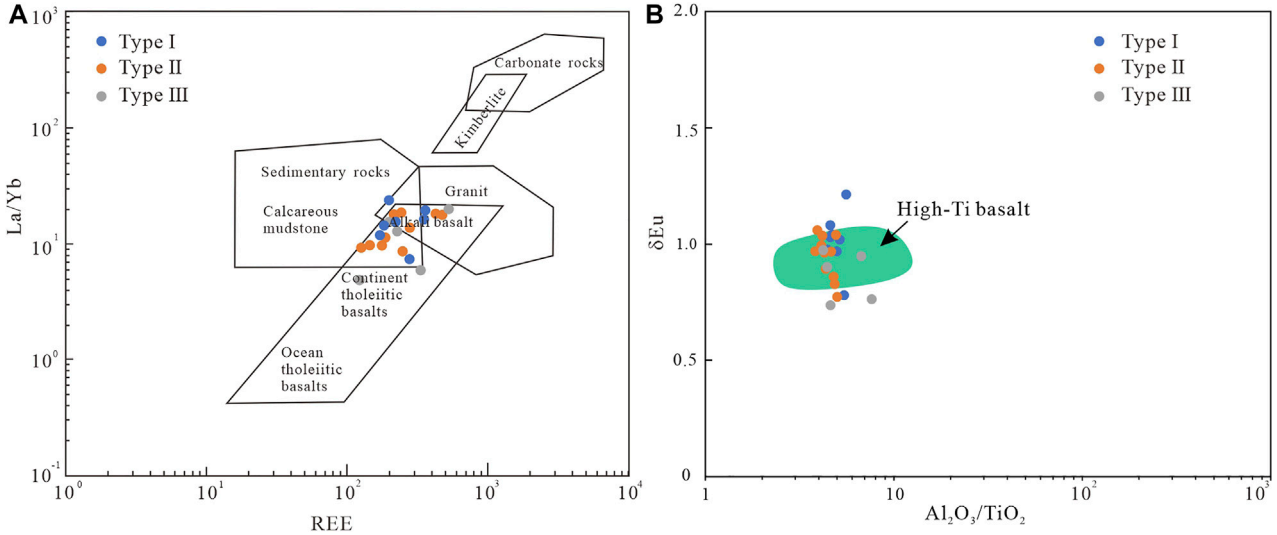

FIGURE 7 | Provenance analysis, **(A)** La/Yb vs. REE diagram; **(B)** δEu vs. Al_2O_3/TiO_2 diagram (data for high-Ti basalt are from Xiao et al., 2004).

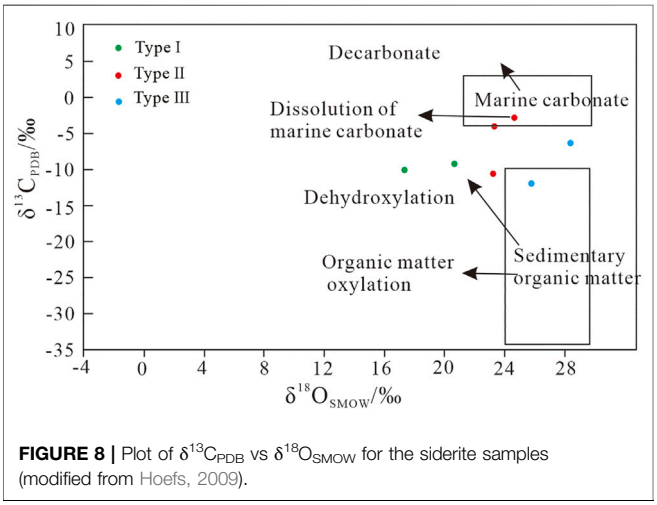

FIGURE 8 | Plot of $\delta^{13}C_{PDB}$ vs $\delta^{18}O_{SMOW}$ for the siderite samples (modified from Hoefs, 2009).

may be sedimentary organic matter and marine carbonate. Microlite siderite is evenly distributed in the strata (**Figure 2**), and its source is more likely sedimentary organic matter, whereas powder crystal siderite is formed by metasomatic calcite or paleontological shell. The CO_2 sources of spheroidal siderite are sedimentary organic matter and marine carbonate rocks, which are affected by different water during diagenesis. Moreover, the analysis results of spheroidal siderite may indicate the genesis of various spheroidal siderite.

5.2 Depositional Conditions of Siderite-Bearing Strata

Elemental concentration ratios such as Sr/Ba, Sr/Cu, V/(V+Ni) in clastic rocks can indicate the depositional conditions (Hatch and Leventhal, 1992; Mongenot et al., 1996; Rimmer et al., 2004; Akinlua et al., 2010; Zhao et al., 2016; Xu et al., 2017). Generally, Sr is enriched in the marine, and Ba is concentrated in the continental deposition. The Sr/Ba ratio reflects the influence degree by seawater and freshwater during the deposition period. The higher the value, the stronger the influence degree by seawater (Johnsson, 1993; Armstrong-Altrin et al., 2015). The whole-rock Sr/Ba value of samples with gelatinous siderite ranged from 1.14 to 2.18, with an average of 1.45 (**Figure 9A**). In addition, the gelatinous siderite-bearing strata contain glauconite (**Figure 2D**), indicating that the gelatinous siderite is strongly affected by seawater (Odin and Matter, 1981; Johnsson, 1993; Armstrong-Altrin et al., 2015; Banerjee et al., 2016). The whole-rock Sr/Ba value of samples with microlite-powder crystal siderite ranges from 0.5 to 0.9, with an average of 0.74, indicating that this kind of siderite was deposited under the joint action of seawater and freshwater (Johnsson, 1993; Armstrong-Altrin et al., 2015). The whole-rock Sr/Ba value of samples with sphaerosiderites ranged from 0.39 to 1.08, indicating that the paleosalinity of the water column during the sedimentary period of this type was relatively low, and the morphology was different under different paleosalinity.

The Sr/Cu ratio can indicate the paleoclimate (Roy and Roser, 2013; Sarki Yandoka et al., 2015). Under warm and humid climatic conditions, sediments usually show a low Sr/Cu ratio (Roy and Roser, 2013; Sarki Yandoka et al., 2015). **Figure 9B** shows that the whole-rock Sr/Cu of samples with gelatinous siderite ranges from 1.38 to 6.30 (mostly from 1 to 5), with an average of 3.21; that of the microlite-powder crystal siderite ranges from 1.33 to 3.97, with an average of 2.42. The spheroidal siderite has an Sr/Cu ranging from 1.69 to 3.29, and there is no significant difference in the value. The chemical index of alteration (CIA) indicates that the paleoclimate where types II and III siderite formed is warm and humid. The CIA of gelatinous siderite is greater than 80,

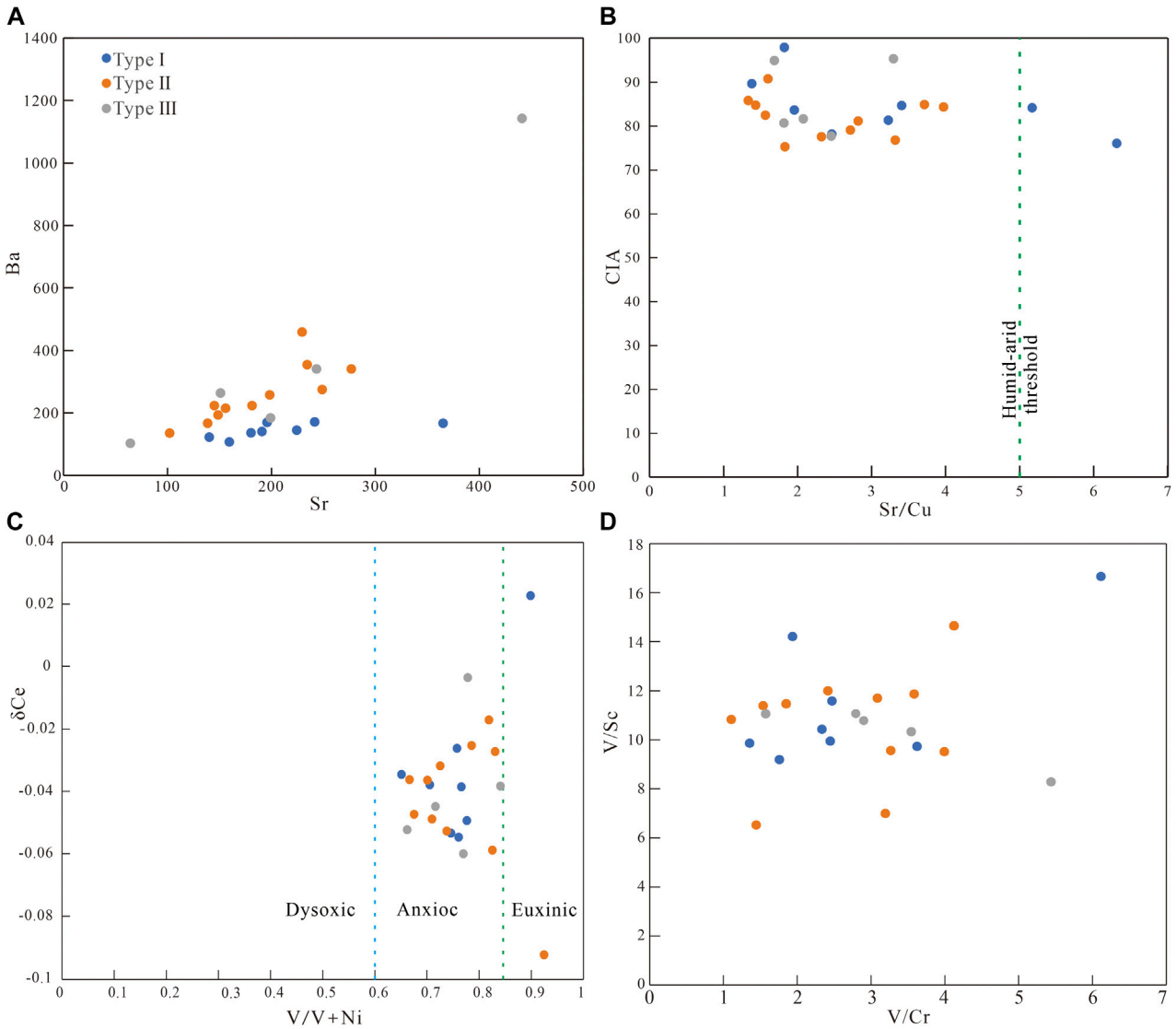

FIGURE 9 | Distribution diagrams of paleosalinity and redox proxies for siderite-bearing strata samples.

reflecting the hot and humid climate (Nesbitt and Young, 1982; McLennan, 1993).

The concentrations of V, Ni, and Ce in fine-grained sediments are sensitive to redox conditions and can help to characterize the depositional conditions (Wright et al., 1987; Jones and Manning, 1994; Holser, 1997; Chen et al., 2015). In general, the value of δ Ce > −0.1 indicates the anoxic condition, and less than −0.1 indicates the oxic condition (Wright et al., 1987; Holser, 1997; Chen et al., 2015). V/(V+Ni) ratios >0.84, 0.84–0.6, and <0.6 represent euxinic, anoxic, and dysoxic conditions, respectively (Hatch and Leventhal, 1992; Zhao et al., 2016; Xu et al., 2017). Moreover, V/Sc and V/Cr ratios can also provide information of depositional conditions (Jones and Manning, 1994; Rimmer et al., 2004). **Figure 9C** shows that the whole-rock δ Ce values of all samples are greater than −0.1, indicating that the water column in the sedimentary period was anoxic. The whole-rock V/(V+Ni) ratio of most samples is between 0.6 and 0.84, showing that they were formed under the weak reducing condition with weak stratification of the water column (Hatch and Leventhal, 1992; Zhao et al., 2016; Xu et al., 2017). The whole-rock V/Sc value of the samples varies little (**Figure 9D**). Among them, the type I siderite was 9.19 to 16.66, with a mean value of 11.45; the types II and III siderite ranges from 6.53 to 14.65 and 8.29 to 11.07, with an average value of 10.59 and 10.31, respectively. It shows that most siderite-bearing strata are formed in a weak reduction environment (Jones and Manning, 1994). The whole-rock V/Cr values of gelatinous siderite, microcrystal-silty siderite, and spheroidal siderites are 1.36 to 6.12, 1.11 to 4.12, 1.57 to 5.44, with an average value of 2.76, 2.69, and 3.25, respectively. Although the V/Cr values of some samples are low, the existing geochemical indicators show that most siderite-bearing strata

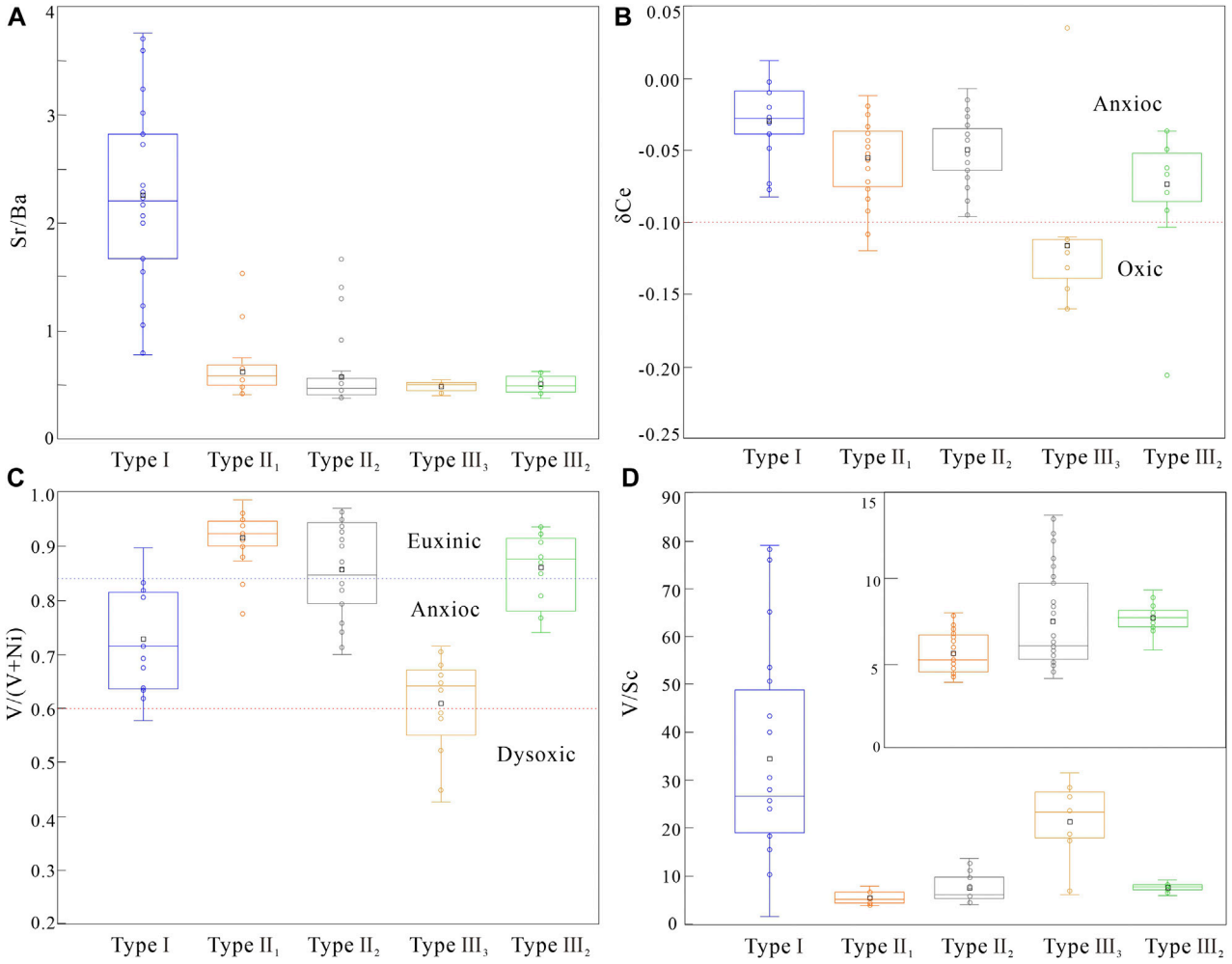

FIGURE 10 | *In situ* geochemical characteristics of different types of siderite.

samples are formed in a weak reduction to reduction environment (Jones and Manning, 1994; Rimmer et al., 2004).

5.3 Diagenetic Environment and Genesis of Siderite

Siderite is an authigenic mineral, and thus, different micro forms of siderite retain the information of diagenetic water during its formation.

According to the *in situ* test results, the $FeCO_3$ content of type I siderite is the lowest among the three types. The Al and Si contents are high, and the Al/Si ratio is almost the same, close to 0.9. The results show that gelatinous siderite is symbiotic with fine clay. The Sr/Ba value of each spot in type I siderite is between 0.79 and 3.75, with an average of 2.26 (**Figure 10A**), higher than that of the whole rock (**Figure 9A**). These characteristics indicate that the diagenetic fluid is mainly seawater with high paleosalinity, similar to sedimentary water (Johnsson, 1993; Armstrong-Altrin et al., 2015). The average value of δ Ce is −0.03 (**Figure 10B**), which is similar to the whole rock (**Table 2**). The mean value of V/(V+Ni) of the *in situ* mineral is 0.73. Compared with the whole-rock V/(V+Ni) of the corresponding samples, the V/(V+Ni) value of the *in situ* mineral is basically unchanged. The value of V/Sc of the *in situ* mineral is 10.25 to 79.02, with an average of 35.85, significantly higher than the whole rock (**Figure 10D**). These characters indicate that the type I siderite was formed in an early diagenetic environment, and the diagenetic water is mainly reduced and stagnant seawater (Hatch and Leventhal, 1992; Zhao et al., 2016). During the gelatinous siderite formation, the content of the clastic particles is low, and a large number of clay minerals are distributed in the sediments. During the syngenetic stage, the cryptic crystalline siderite precipitates from the seawater and filled in the limited space as cements.

The $FeCO_3$ content of type II_1 siderite is higher than that of type I siderite, whereas the content of Al and Si is lower, with average Al/Si value of 0.41. The type II_1 siderite appears hypidiomorphic granular aggregates, and the crystal morphology is not obvious, only with the boundary between crystal particles vaguely observed (**Figure 2F**). Moreover, the clay mineral content in the pores is relatively low, and the siderite is

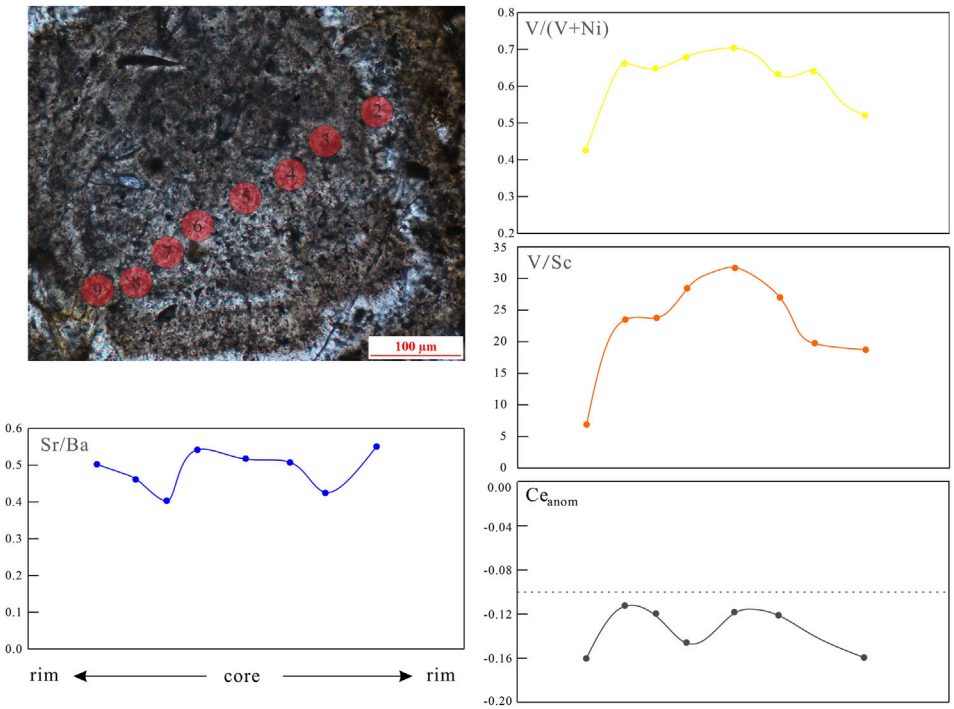

FIGURE 11 | Variation curves from center to edge of concentric siderite.

relatively pure. The above characteristics indicate that the microlite siderite is likely to be formed in the original intergranular pores. The average *in situ* Sr/Ba of type II_1 siderite is 0.64, and that of the whole rock is 0.66. There is almost no difference between them, meaning that the paleosalinity of the diagenetic water is similar to the sedimentary water body, that is, saltwater (Johnsson, 1993; Armstrong-Altrin et al., 2015). The average value of δ Ce in *in situ* mineral is −0.06, V/(V+Ni) is 0.93, and V/Sc is 4.80; δ Ce and V/(V+Ni) are similar to the average values of whole rock, whereas V/Sc is obviously lower than the average value of whole rock (**Figure 10D**; the average value of whole rock is 11.58). Therefore, the diagenetic water where type II_1 siderite formed is weakly reduced (Hatch and Leventhal, 1992; Jones and Manning, 1994; Rimmer et al., 2004; Zhao et al., 2016). The diagenetic environment of type II_1 siderite is similar to its sedimentary environment. It is a saltwater fluid with weak oxidation–reduction, and the diagenetic water is likely to be primary porewater. During the sedimentation of the strata with type II_1 siderite, the fluid washed the original pores, and the intergranular clay minerals decreased. The primary porewater through layers provides Fe-forming materials for the crystallization of siderite, which promotes the precipitation of siderite in intergranular pores and forms microlite siderite. However, because of the limited crystallization space, the siderite is filled in the pores and developed in the form of microlite siderite aggregate.

The type II_1 siderite appears as silty-sized crystal aggregates, and some develop into petal-like siderite (**Figures 2L,J**). The $FeCO_3$ content is approximately 80 wt%. The Sr/Ba ranges from 0.38 to 1.66, with an average value of 0.58 (**Figure 10A**), different from the average Sr/Ba of the whole rock of 0.96. The Sr/Ba value indicates that the type II_2 siderite was transformed by freshwater in the later diagenetic stage (Johnsson, 1993; Armstrong-Altrin et al., 2015). The *in situ* V/Sc values are 2.9 to 9.0, with an average of 5.24, which are lower than those of the whole rock (**Figure 9B**) (averagely 11.52). The V/(V+Ni) value is between 0.7 and 0.97 (**Figure 10C**), with an average of 0.85, which is higher than the whole rock (average 0.75). The δ Ce values range from −0.1 to −0.01 (**Figure 10B**), which is slightly lower than whole rock (from −0.03 to −0.06, average −0.04). These characteristics reveal the diagenetic water where type II_2 siderite formed is different from its sedimentary water; that is, the diagenetic water is not seawater sealed in sedimentary period or primary porewater, but relatively freshwater with weak oxidation to weak reduction (Hatch and Leventhal, 1992; Jones and Manning, 1994; Rimmer et al., 2004). During the burial period, the siderite had been transformed by the diagenetic fluid, which promoted the recrystallization of siderite crystals with smaller particles formed in the sedimentary period and formed powder crystal siderite with silty size and better crystal morphology.

The type III siderite can be divided into three subtypes based on microscopic morphology. According to the observed type III_1 siderite, the morphologies range from powder crystals through fan-shaped to petal-like morphologies (**Figures 2K,L**); it is likely to be formed by a single crystal, and the morphology is affected by pores and diagenetic fluid (Passey, 2014). According to the *in situ* results (**Figure 10**), the Sr/Ba ranges from 0.38 to 0.63, indicating

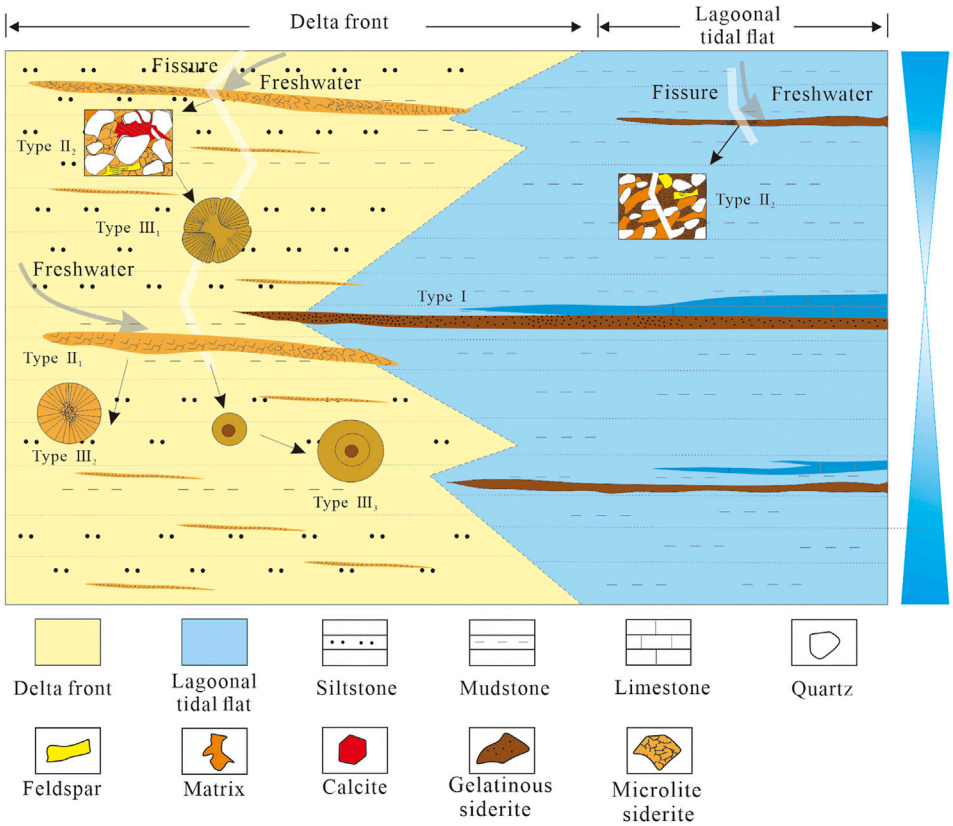

FIGURE 12 | Evolution model of different types of Siderite.

that the formation environment was affected by freshwater. The *in situ* V/Sc, V/(V+Ni), and δ Ce values are 5.6 to 9.3, 0.74 to 0.94, and −0.21 to −0.04, respectively. These characteristics indicate that the type III_2 siderite grows radially around the core with weak oxidation to weak reduction. The variation curves of many geochemical indexes from the core to the rim of type III_3 siderite show obvious symmetry (**Figure 11**), indicating that its growth is slow and continuous and carried out together with the diagenesis. Under the repeated action of diagenetic fluid, the type III_3 siderite grows in a circle around the cryptocrystalline core in a fluid with the weak oxidation–reduction property.

5.4 Evolution Model of Siderite and Geological Significance

Siderite in the study area shows various forms and has been affected by sedimentary environment and diagenetic environment. Regarding the sedimentary environment, the Upper Permian coal-bearing strata developed under carbonate tidal flat-barrier-lagoon-shallow delta conditions (Wang et al., 2011; Shen et al., 2016; Shen et al., 2019; Qin et al., 2018), and the climate was hot and humid. Such sedimentary condition was beneficial to the formation of siderite (Bercovici et al., 2015). The development and evolution model of siderite is shown in **Figure 12**. The formation of type I siderite is strongly affected by seawater during transgression, and the sedimentary water is stagnant seawater. During diagenesis, the diagenetic water along the fissures and beddings promoted the recrystallization of the gelatinous siderite to form the powder siderite (**Figure 12**). The sedimentary water of type II siderite gradually changed from seawater to brackish water in the transitional environment. During diagenesis, the diagenetic fluid of freshwater promoted the recrystallization of siderite along fissures and beddings or metasomatism with calcite to evolve into type II_2 siderite and sometimes into petal-like siderite (**Figure 12**). The type III_2 siderite grows radially around the core. The type III_3 siderite grows in a circle around the cryptocrystalline core in a relatively active fluid with weak oxidation–reduction under the repeated diagenetic fluid. Under the influence of multistage diagenetic fluid, the type III_3 siderite grows around the cryptocrystalline core.

The formation of siderite is obviously controlled by the different sedimentary and diagenetic environments. Among them, types I and II_1 siderite mainly formed in the syndiagenetic and early diagenetic stages, and their morphology is controlled by the sedimentary environment. Therefore, types I and II_1 siderite can indicate the sedimentary environments. Gelatinous siderite was most affected by seawater, mostly formed in the transgression or near the maximum flooding surface (Shen et al., 2019; Zhang et al., 2020).

Microlite siderite was influenced by freshwater during its formation and was most developed in the early stage of transgression or high-stand system tract.

6 CONCLUSION

Based on the morphology of siderite in coal-bearing series, it can be divided into three types and six subtypes. There is barely any difference in the sedimentary sources of various siderite-bearing strata, which are Emeishan high-titanium basalt developed in the west of the study area. Type I siderite CO_2 comes from sedimentary organic matter. Types II and III siderite CO_2 is mainly derived from sedimentary organic matter and marine carbonate.

The most significant difference in the sedimentary period of various siderite-bearing strata lies in the influence degree of seawater. Among them, type I siderite-bearing strata are strongly affected by seawater, whereas types II and III siderite-bearing strata are affected by seawater and freshwater. Different types of siderite bearing strata are formed in depositional conditions from weak oxidation to weak reduction.

The *in situ* results show that types I and II_1 siderites were formed in the early diagenetic stage. The diagenetic water of type I siderite is sedimentary seawater, and type II_1 siderite is mainly primary porewater. The diagenetic water of type II_2 siderite is freshwater, and type III is multistage fluid.

The siderite morphologies are controlled by the sedimentary environment and diagenetic environment. Among them, gelatinous siderite and microlite siderite are mainly formed in the syndiagenetic stage and early diagenetic stage, thus indicating the sedimentary environment. Gelatinous siderite is strongly influenced by seawater and is mainly formed in the carbonate tidal flat and barrier lagoon. Microlite siderite is formed in the shallow delta with relatively low sea level by the interaction of seawater and freshwater.

DATA AVAILABILITY STATEMENT

The raw data supporting the conclusion of this article will be made available by the authors, without undue reservation.

AUTHOR CONTRIBUTIONS

TY: Conceptualization, methodology, writing—original draft. YS: Conceptualization, supervision, project administration, funding acquisition. YQ: Writing—original draft, visualization,investigation. YiZ: Software, validation. JJ: Investigation, resources, supervision. YoZ: Writing-reviewing and Editing. YlZ: Writing-reviewing and Editing. YfZ: Data curation, validation.

FUNDING

Financial support for this work was provided by the National Natural Science Foundation of China (Nos. 42172186 and 41872168) and the Priority Academic Program Development of the Jiangsu Higher Education Institutions (PAPD).

SUPPLEMENTARY MATERIAL

The Supplementary Material for this article can be found online at: https://www.frontiersin.org/articles/10.3389/feart.2021.779991/full#supplementary-material

REFERENCES

Akinlua, A., Adekola, S. A., Swakamisa, O., Fadipe, O. A., and Akinyemi, S. A. (2010). Trace Element Characterisation of Cretaceous Orange Basin Hydrocarbon Source Rocks. *Appl. Geochem.* 25, 1587–1595. doi:10.1016/j.apgeochem.2010.08.008

Allègre, C. J., and Michard, G. (1974). *Introduction to Geochemistry 10 (Geophysics and Astrophysics Monographs)*. Boston, USA: D. Reidel Publishing Company.

Armstrong-Altrin, J. S., Machain-Castillo, M. L., Rosales-Hoz, L., Carranza-Edwards, A., Sanchez-Cabeza, J.-A., and Ruíz-Fernández, A. C. (2015). Provenance and Depositional History of continental Slope Sediments in the Southwestern Gulf of Mexico Unraveled by Geochemical Analysis. *Continental Shelf Res.* 95, 15–26. doi:10.1016/j.csr.2015.01.003

Banerjee, S., Bansal, U., Pande, K., and Meena, S. S. (2016). Compositional Variability of Glauconites within the Upper Cretaceous Karai Shale Formation, Cauvery Basin, India: Implications for Evaluation of Stratigraphic Condensation. *Sediment. Geology.* 331, 12–29. doi:10.1016/j.sedgeo.2015.10.012

Bercovici, A., Cui, Y., Forel, M.-B., Yu, J., and Vajda, V. (2015). Terrestrial Paleoenvironment Characterization across the Permian-Triassic Boundary in South China. *J. Asian Earth Sci.* 98, 225–246. doi:10.1016/j.jseaes.2014.11.016

Berner, R. A. (1981). A New Geochemical Classification of Sedimentary Environments. *Sepm Jsr* 51, 359–365. doi:10.1306/212F7C7F-2B24-11D7-8648000102C1865D

Boynton, W. V. (1984). Chapter 3 Cosmochemistry of the Rare Earth Elements: Meteorite Studies. *Dev. Geochem.* 2, 63–114. doi:10.1016/B978-0-444-42148-7.50008-3

Chen, J., Algeo, T. J., Zhao, L., Chen, Z.-Q., Cao, L., Zhang, L., et al. (2015). Diagenetic Uptake of Rare Earth Elements by Bioapatite, with an Example from Lower Triassic Conodonts of South China. *Earth-Science Rev.* 149, 181–202. doi:10.1016/j.earscirev.2015.01.013

Choi, K. S., Khim, B. K., and Woo, K. S. (2003). Spherulitic Siderites in the Holocene Coastal Deposits of Korea (Eastern Yellow Sea): Elemental and Isotopic Composition and Depositional Environment. *Mar. Geology.* 202, 17–31. doi:10.1016/s0025-3227(03)00258-5

Chung, S.-L., and Jahn, B.-M. (1995). Plume-lithosphere Interaction in Generation of the Emeishan Flood Basalts at the Permian-Triassic Boundary. *Geol* 23, 889–892. doi:10.1130/0091-7613(1995)023<0889:pliigo>2.3.co;2

Curtis, C. D., Coleman, M. L., and Love, L. G. (1986). Pore Water Evolution during Sediment Burial from Isotopic and mineral Chemistry of Calcite, Dolomite and Siderite Concretions. *Geochimica et Cosmochimica Acta.* 50, 2321–2334. doi:10.1016/0016-7037(86)90085-2

Dai, S., Chekryzhov, I. Y., Seredin, V. V., Nechaev, V. P., Graham, I. T., Hower, J. C., et al. (2016). Metalliferous Coal Deposits in East Asia (Primorye of Russia and South China): A Review of Geodynamic Controls and Styles of Mineralization. *Gondwana Res.* 29, 60–82. doi:10.1016/j.gr.2015.07.001

Dai, S., Ward, C. R., Graham, I. T., French, D., Hower, J. C., Zhao, L., et al. (2017). Altered Volcanic Ashes in Coal and Coal-Bearing Sequences: a Review of Their

Nature and Significance. *Earth-Science Rev.* 175, 44–74. doi:10.1016/j.earscirev.2017.10.005

El Albani, A., Vachard, D., Kuhnt, W., and Thurow, J. (2001). The Role of Diagenetic Carbonate Concretions in the Preservation of the Original Sedimentary Record. *Sedimentology* 48 (4), 875–886. doi:10.1046/j.1365-3091.2001.00398.x

Haese, R. R., Wallmann, K., Dahmke, A., Kretzmann, U., Müller, P. J., and Schulz, H. D. (1997). Iron Species Determination to Investigate Early Diagenetic Reactivity in marine Sediments. *Geochimica et Cosmochimica Acta* 61 (Issue 1), 63–72. doi:10.1016/S0016-7037(96)00312-2

Hatch, J. R., and Leventhal, J. S. (1992). Relationship between Inferred Redox Potential of the Depositional Environment and Geochemistry of the Upper Pennsylvanian (Missourian) Stark Shale Member of the Dennis Limestone, Wabaunsee County, Kansas, U.S.A. *Chem. Geology.* 99, 65–82. doi:10.1016/0009-2541(92)90031-Y

He, B., Xu, Y.-G., Chung, S.-L., Xiao, L., and Wang, Y. (2003). Sedimentary Evidence for a Rapid, Kilometer-Scale Crustal Doming Prior to the Eruption of the Emeishan Flood Basalts. *Earth Planet. Sci. Lett.* 213, 391–405. doi:10.1016/S0012-821X(03)00323-6

He, B., Xu, Y.-G., Huang, X.-L., Luo, Z.-Y., Shi, Y.-R., Yang, Q.-J., et al. (2007). Age and Duration of the Emeishan Flood Volcanism, SW China: Geochemistry and SHRIMP Zircon U-Pb Dating of Silicic Ignimbrites, post-volcanic Xuanwei Formation and clay Tuff at the Chaotian Section. *Earth Planet. Sci. Lett.* 255, 306–323. doi:10.1016/j.epsl.2006.12.021

He, Q., Dong, T., He, S., Zhai, G., Guo, X., Hou, Y., et al. (2020). Sedimentological and Geochemical Characterization of the Upper Permian Transitional Facies of the Longtan Formation, Northern Guizhou Province, Southwest China: Insights into Paleo-Environmental Conditions and Organic Matter Accumulation Mechanisms. *Mar. Pet. Geology.* 118, 104446. doi:10.1016/j.marpetgeo.2020.104446

Hiatt, E. E., Pufahl, P. K., and Guimarães da Silva, L. (2020). Iron and Phosphorus Biochemical Systems and the Cryogenian-Ediacaran Transition, Jacadigo basin, Brazil: Implications for the Neoproterozoic Oxygenation Event. *Precambrian Res.* 337, 105533. doi:10.1016/j.precamres.2019.105533

Hoefs, J. (2009). *Stable Isotope Geochemistry*. Berlin: Springer-Verlag.

Holser, W. (1997). Evaluation of the application of rare-earth elements to paleoceanography. *Palaeogeogr. Palaeocl.* 132, 309–323. doi:10.1016/S0031-0182(97)00069-2

Johnsson, M. J. (1993). *The System Controlling the Composition of Clastic Sediments*, 284. Pennsylvania: Geological Society of America, 1–20. doi:10.1130/SPE284-p1

Jones, B., and Manning, D. A. C. (1994). Comparison of Geochemical Indices Used for the Interpretation of Palaeoredox Conditions in Ancient Mudstones. *Chem. Geology.* 111, 111–129. doi:10.1016/0009-2541(94)90085-X

Laenen, B., and De Craen, M. (2004). Eogenetic Siderite as an Indicator for Fluctuations in Sedimentation Rate in the Oligocene Boom Clay Formation (Belgium). *Sediment. Geology.* 163, 165–174. doi:10.1016/S0037-0738(03)00177-5

Lim, D. I., Jung, H. S., Yang, S. Y., and Yoo, H. S. (2004). Sequential Growth of Early Diagenetic Freshwater Siderites in the Holocene Coastal Deposits, Korea. *Sediment. Geology.* 169, 107–120. doi:10.1016/j.sedgeo.2004.05.002

Liu, J., Nechaev, V. P., Dai, S., Song, H., Nechaeva, E. V., Jiang, Y., et al. (2020). Evidence for Multiple Sources for Inorganic Components in the Tucheng Coal deposit, Western Guizhou, China and the Lack of Critical-Elements. *Int. J. Coal Geology.* 223, 103468. doi:10.1016/j.coal.2020.103468

Liu, J., Song, H., Dai, S., Nechaev, V. P., Graham, I. T., French, D., et al. (2019). Mineralization of REE-Y-Nb-Ta-Zr-Hf in Wuchiapingian Coals from the Liupanshui Coalfield, Guizhou, Southwestern China: Geochemical Evidence for Terrigenous Input. *Ore Geology. Rev.* 115, 103190. doi:10.1016/j.oregeorev.2019.103190

Liu, Y.-F., Qi, H.-W., Bi, X.-W., Hu, R.-Z., Qi, L.-K., Yin, R.-S., et al. (2021). Two Types of Sediment-Hosted Pb-Zn Deposits in the Northern Margin of Lanping basin, SW China: Evidence from Sphalerite Trace Elements, Carbonate C-O Isotopes and Molybdenite Re-os Age. *Ore Geology. Rev.* 131, 104016. doi:10.1016/j.oregeorev.2021.104016

Ludvigson, G. A., González, L. A., Metzger, R. A., Witzke, B. J., Brenner, R. L., Murillo, A. P., et al. (1998). Meteoric Sphaerosiderite Lines and Their Use for Paleohydrology and Paleoclimatology. *Geol* 26, 1039–1042. doi:10.1130/0091-7613(1998)026<1039:mslatu>2.3.co;2

McLennan, S. M., Hemming, S., McDaniel, D. K., and Hanson, G. N. (1993). *Geochemical Approaches to Sedimentation, Provenance, and Tectonics*, 284. New York, NY: Special Paper of the Geological Society of America, 21–40. doi:10.1130/SPE284-p21

McLennan, S. M. (1993). Weathering and Global Denudation. *J. Geology.* 101, 295–303. doi:10.1086/648222

Mongenot, T., Tribovillard, N.-P., Desprairies, A., Lallier-Vergès, E., and Laggoun-Defarge, F. (1996). Trace Elements as Palaeoenvironmental Markers in Strongly Mature Hydrocarbon Source Rocks: the Cretaceous La Luna Formation of Venezuela. *Sediment. Geology.* 103, 23–37. doi:10.1016/0037-0738(95)00078-X

Mozley, P. S. (1989). Relation between Depositional Environment and the Elemental Composition of Early Diagenetic Siderite. *Geol* 17, 704–706. doi:10.1130/0091-7613(1989)017<0704:rbdeat>2.3.co;2

Mozley, P. S., and Wersin, P. (1992). Isotopic Composition of Siderite as an Indicator of Depositional Environment. *Geol* 20, 817–820. doi:10.1130/0091-7613(1992)020<0817:icosaa>2.3.co;2

Nesbitt, H. W., and Young, G. M. (1982). Early Proterozoic Climates and Plate Motions Inferred from Major Element Chemistry of Lutites. *Nature* 299, 715–717. doi:10.1038/299715a0

Odin, G. S., and Matter, A. (1981). De Glauconiarum Origine. *Sedimentology* 28, 611–641. doi:10.1111/j.1365-3091.1981.tb01925.x

Ohmoto, H. (1972). Systematics of Sulfur and Carbon Isotopes in Hydrothermal Ore Deposits. *Econ. Geol.* 67 (5), 551–578. doi:10.2113/gsecongeo.67.5.551

Passey, S. R. (2014). The Habit and Origin of Siderite Spherules in the Eocene Coal-Bearing Prestfjall Formation, Faroe Islands. *Int. J. Coal Geology.* 122, 76–90. doi:10.1016/j.coal.2013.12.009

Passey, S., and Jolley, D. (2009). A revised lithostratigraphic nomenclature for the Palaeogene Faroe Islands Basalt Group, NE Atlantic Ocean. *Earth Env. Sci. T. R. So.* 99, 127–158. doi:10.1017/S1755691009008044

Phillips, S. C., Hong, W.-L., Johnson, J. E., Fahnestock, M. F., and Bryce, J. G. (2018). Authigenic Carbonate Formation Influenced by Freshwater Inputs and Methanogenesis in Coal-Bearing Strata Offshore Shimokita, Japan (IODP Site C0020). *Mar. Pet. Geology.* 96, 288–303. doi:10.1016/j.marpetgeo.2018.06.007

Qin, Y., Moore, T. A., Shen, J., Yang, Z., Shen, Y., and Wang, G. (2018). Resources and Geology of Coalbed Methane in China: A Review. *Int. Geology. Rev.* 60, 777–812. doi:10.1080/00206814.2017.1408034

Rimmer, S., Thompson, J., Goodnight, S., and Robl, T. (2004). Multiple Controls on the Preservation of Organic Matter in Devonian-Mississippian marine Black Shales: Geochemical and Petrographic Evidence. *Palaeogeogr. Palaeoclimatol. Palaeoecol.* 215, 125–154. doi:10.1016/s0031-0182(04)00466-3

Rodrigues, A. G., De Ros, L. F., Neumann, R., and Borghi, L. (2015). Paleoenvironmental Implications of Early Diagenetic Siderites of the Paraíba Do Sul Deltaic Complex, Eastern Brazil. *Sediment. Geology.* 323, 15–30. doi:10.1016/j.sedgeo.2015.04.005

Roy, D., and Roser, B. (2013). Climatic Control on the Composition of Carboniferous-Permian Gondwana Sediments, Khalaspir basin, Bangladesh. *Gondwana Res.* 23, 1163–1171. doi:10.1016/j.gr.2012.07.006

Sánchez-Román, M., Fernández-Remolar, D., Amils, R., Sánchez-Navas, A., Schmid, T., Martin-Uriz, P. S., et al. (2014). Microbial Mediated Formation of Fe-Carbonate Minerals under Extreme Acidic Conditions. *Sci. Rep.* 4, 4767. doi:10.1038/srep04767

Sarki Yandoka, B., Abdullah, W., Abubakar, M., Hakimi, M., and Adegoke, A. (2015). Geochemical characterisation of Early Cretaceous lacustrine sediments of Bima Formation, Yola sub-basin, Northern Benue Trough, NE Nigeria: Organic matter input, preservation, Paleoenvironment and Palaeoclimatic conditions. *Mar. Petrol. Geol.* 61, 82–94. doi:10.1016/j.marpetgeo.2014.12.010

Shao, Y., Guo, Y., Qin, Y., Shen, Y., and Tian, L. (2011). Distribution Characteristic and Geological Significance of Rare Earth Elements in Lopingian Mudstone of Permian, Panxian County, Guizhou Province. *Mining Sci. Tech. (China)* 21 (4), 469–476. doi:10.1016/j.mstc.2011.06.002

Shen, Y. L., Qin, Y., Li, Z. F., Jin, J., Wei, Z. H., Zheng, J., et al. (2017). The Sedimentary Origin and Geological Significance of Siderite in the Longtan Formation of Western Guizhou Province. *Earth Sci. Front.* 24, 152–161. (in Chinese with English abstract). doi:10.13745/j.esf.yx.2016-11-51

Shen, Y., Qin, Y., Guo, Y., Yi, T., Yuan, X., and Shao, Y. (2016). Characteristics and Sedimentary Control of a Coalbed Methane-Bearing System in Lopingian (Late

Permian) Coal-Bearing Strata of Western Guizhou Province. *J. Nat. Gas Sci. Eng.* 33, 8–17. doi:10.1016/j.jngse.2016.04.047

Shen, Y., Qin, Y., Wang, G. G. X., Xiao, Q., Shen, J., Jin, J., et al. (2019). Sealing Capacity of Siderite-Bearing Strata: the Effect of Pore Dimension on Abundance and Micromorphology Type of Siderite in the Lopingian (Late Permian) Coal-Bearing Strata, Western Guizhou Province. *J. Pet. Sci. Eng.* 178, 180–192. doi:10.1016/j.petrol.2019.03.032

Spears, D. A., and Rice, C. M. (1973). An Upper Carboniferous Tonstein of Volcanic Origin. *Sedimentology* 20, 281–294. doi:10.1111/j.1365-3091.1973.tb02050.x

Taylor, S. R., and McLennan, S. M. (1985). *The Continental Crust: Its Composition and Evolution: An Examination of the Geochemical Record Preserved in Sedimentary Rocks*. Oxford: Blackwell Scientific, 312.

Tribovillard, N., Algeo, T. J., Lyons, T., and Riboulleau, A. (2006). Trace Metals as Paleoredox and Paleoproductivity Proxies: An Update. *Chem. Geology.* 232, 12–32. doi:10.1016/j.chemgeo.2006.02.012

Uysal, I. T., Golding, S. D., and Glikson, M. (2000). Petrographic and Isotope Constraints on the Origin of Authigenic Carbonate Minerals and the Associated Fluid Evolution in Late Permian Coal Measures, Bowen Basin (Queensland), Australia. *Sediment. Geology.* 136, 189–206. doi:10.1016/S0037-0738(00)00097-X

Veizer, J., Holser, W. T., and Wilgus, C. K. (1980). Correlation of and Secular Variations. *Geochimica et Cosmochimica Acta* 44, 579–587. doi:10.1016/0016-7037(80)90250-1

Wang, H., Shao, L., Hao, L., Zhang, P., Glasspool, I. J., Wheeley, J. R., et al. (2011). Sedimentology and Sequence Stratigraphy of the Lopingian (Late Permian) Coal Measures in Southwestern China. *Int. J. Coal Geology.* 85, 168–183. doi:10.1016/j.coal.2010.11.003

Weibel, R., Lindström, S., Pedersen, G. K., Johansson, L., Dybkjær, K., Whitehouse, M. J., et al. (2016). Groundwater Table Fluctuations Recorded in Zonation of Microbial Siderites from End-Triassic Strata. *Sediment. Geology.* 342, 47–65. doi:10.1016/j.sedgeo.2016.06.009

Wittkop, C., Teranes, J., Lubenow, B., and Dean, W. (2014). Carbon- and Oxygen-Stable Isotopic Signatures of Methanogenesis, Temperature, and Water Column Stratification in Holocene Siderite Varves. *Chem. Geol.* 389, 153–166. doi:10.1016/j.chemgeo.2014.09.016

Wright, J., Schrader, H., and Holser, W. T. (1987). Paleoredox Variations in Ancient Oceans Recorded by Rare Earth Elements in Fossil Apatite. *Geochimica et Cosmochimica Acta* 51, 631–644. doi:10.1016/0016-7037(87)90075-5

Xiao, L., Xu, Y. G., Mei, H. J., Zheng, Y. F., He, B., and Pirajno, F. (2004). Distinct Mantle Sources of Low-Ti and High-Ti Basalts from the Western Emeishan Large Igneous Province, SW China: Implications for Plume-Lithosphere Interaction. *Earth Planet. Sci. Lett.* 228, 525–546. doi:10.1016/j.epsl.2004.10.002

Xie, G., Shen, Y., Liu, S., and Hao, W. (2018). Trace and Rare Earth Element (REE) Characteristics of Mudstones from Eocene Pinghu Formation and Oligocene Huagang Formation in Xihu Sag, East China Sea Basin: Implications for Provenance, Depositional Conditions and Paleoclimate. *Mar. Pet. Geology.* 92, 20–36. doi:10.1016/j.marpetgeo.2018.02.019

Xu, B., and He, M. (2003). *Coal Geology of Guizhou Province*. Xuzhou, China: China University of Mining and Technology Press.

Xu, Q., Liu, B., Ma, Y., Song, X., Wang, Y., and Chen, Z. (2017). Geological and Geochemical Characterization of Lacustrine Shale: A Case Study of the Jurassic Da'anzhai Member Shale in the central Sichuan Basin, Southwest China. *J. Nat. Gas Sci. Eng.* 47, 124–139. doi:10.1016/j.jngse.2017.09.008

Xu, Y.-G., Chung, S.-L., Shao, H., and He, B. (2010). Silicic Magmas from the Emeishan Large Igneous Province, Southwest China: Petrogenesis and Their Link with the End-Guadalupian Biological Crisis. *Lithos* 119, 47–60. doi:10.1016/j.lithos.2010.04.013

Zhang, T., Shen, Y. L., Li, Z. F., Jin, J., Zong, Y., Liu, J. B., et al. (2018). Genesis of Siderite Precipitated in the Lopingian Coal Measures in Zhijin Mining Area, Western Guizhou. *Geol. J. China Universities* 24, 481–490. (in Chinese with English abstract). doi:10.16108/j.issn1006-7493.2017141

Zhang, Y. J., Shen, Y. L., Yang, T. Y., Zhao, Y., and Tong, G. C. (2020). Development Characteristics of Siderite in the Constraint of Sequence Frame: A Case Study of Late Permian Coal Measures in Panguan Area. *J. China Coal Soc.* 45 (S2), 976–985. (in Chinese with English abstract). doi:10.13225/j.cnki.jccs.2020.0200

Zhao, J., Jin, Z., Jin, Z., Geng, Y., Wen, X., and Yan, C. (2016). Applying Sedimentary Geochemical Proxies for Paleoenvironment Interpretation of Organic-Rich Shale Deposition in the Sichuan Basin, China. *Int. J. Coal Geology.* 163, 52–71. doi:10.1016/j.coal.2016.06.015

Conflict of Interest: YoZ was employed by the company Sinopec Shengli Oilfield Administration Bureau Co., Ltd. YiZ was employed by the company Sinopec Xinjiang Xinchun Petroleum Development Co., Ltd.

The remaining authors declare that the research was conducted in the absence of any commercial or financial relationships that could be construed as a potential conflict of interest.